

FEASTS and MHONGOOSE: HI Column Density Distribution at $z=0$ for $N_{\text{HI}} > 10^{17.8} \text{ cm}^{-2}$

JING WANG (王菁),¹ XUCHEN LIN (林旭辰),¹ ZE-ZHONG LIANG (梁泽众),¹ W.J.G. DE BLOK,^{2,3,4} HONG GUO (郭宏),⁵ ZHIJIE QU (屈稚杰),⁶ CÉLINE PÉROUX,^{7,8} KENTARO NAGAMINE,^{9,10,11,12,13} LUIS C. HO (何子山),¹ DONG YANG (杨冬),¹ SIMON WENG,^{14,15,16} CLAUDIA DEL P. LAGOS,^{17,15,18} XINKAI CHEN (陈新凯),¹ GEORGE HEALD,¹⁹ J. HEALY,^{2,20,21} QIFENG HUANG (黄齐丰),¹ PETER KAMPHUIS,²² D. KLEINER,²³ DI LI (李葭),^{24,25} SIQI LIU (刘思琦),^{1,26} F. M. MACCAGNI,²⁷ LISTER STAVELEY-SMITH,¹⁷ ZHERONG SU (苏哲容),²⁸ FREEKE VAN DE VOORT,²⁹ FABIAN WALTER,^{30,31} FANGXIONG ZHONG (钟芳雄),³² AND SIWEI ZOU (邹思蔚)^{33,34}

¹ Kavli Institute for Astronomy and Astrophysics, Peking University, Beijing 100871, China

²Netherlands Institute for Radio Astronomy (ASTRON), Oude Hoogeveensedijk 4, 7991 PD Dwingeloo, the Netherlands

³Dept. of Astronomy, Univ. of Cape Town, Private Bag X3, Rondebosch 7701, South Africa

⁴Kapteyn Astronomical Institute, University of Groningen, PO Box 800, 9700 AV Groningen, The Netherlands

⁵Shanghai Astronomical Observatory, Chinese Academy of Sciences, Shanghai 200030, People's Republic of China

⁶Department of Astronomy and Astrophysics, The University of Chicago, 5640 S. Ellis Avenue, Chicago, IL 60637, USA

⁷European Southern Observatory, Karl-Schwarzschildstrasse 2, D-85748 Garching bei München, Germany

⁸Aix Marseille Université, CNRS, LAM (Laboratoire d'Astrophysique de Marseille) UMR 7326, F-13388 Marseille, France

⁹Theoretical Astrophysics, Department of Earth & Space Science, Graduate School of Science, The University of Osaka, 1-1 Machikaneyama, Toyonaka, Osaka 560-0043, Japan

¹⁰Theoretical Joint Research, Forefront Research Center, Graduate School of Science, The University of Osaka, 1-1 Machikaneyama, Toyonaka, Osaka 560-0043, Japan

¹¹Kavli IPMU (WPI), UTIAS, The University of Tokyo, Kashiwa, Chiba 277-8583, Japan

¹²Department of Physics & Astronomy, University of Nevada, Las Vegas, 4505 S. Maryland Pkwy, Las Vegas, NV 89154-4002, USA

¹³Nevada Center for Astrophysics, University of Nevada, Las Vegas, 4505 S. Maryland Pkwy, Las Vegas, NV 89154-4002, USA

¹⁴Sydney Institute for Astronomy, School of Physics A28, University of Sydney, NSW 2006, Australia

¹⁵ARC Centre of Excellence for All-Sky Astrophysics in 3 Dimensions (ASTRO 3D), Australia

¹⁶ATNF, CSIRO Space and Astronomy, PO Box 76, Epping, NSW 1710, Australia

¹⁷International Centre for Radio Astronomy Research, University of Western Australia, 35 Stirling Highway, Crawley, WA 6009, Australia

¹⁸Cosmic Dawn Center (DAWN), Denmark

¹⁹CSIRO, Space and Astronomy, PO Box 1130, Bentley, WA 6102, Australia

²⁰Jodrell Bank Centre for Astrophysics, School of Physics and Astronomy, University of Manchester, Oxford Road, Manchester M13 9PL, UK

²¹Department of Astronomy, University of Cape Town, Private Bag X3, Rondebosch 7701, South Africa

²²Ruhr University Bochum, Faculty of Physics and Astronomy, Astronomical Institute (AIRUB), 44780, Bochum, Germany

²³Netherlands Institute for Radio Astronomy (ASTRON), Oude Hoogeveensedijk 4, 7991 PD, Dwingeloo, The Netherlands

²⁴New Cornerstone Science Laboratory, Department of Astronomy, Tsinghua University, Beijing 100084, China

²⁵National Astronomical Observatories, Chinese Academy of Sciences, 20A Datun Road, Chaoyang District, Beijing, People's Republic of China

²⁶Department of the Internet of Things and Electronic Engineering, School of Computer and Communication Engineering, University of Science and Technology Beijing, Beijing 100083, China.

²⁷INAF - Osservatorio Astronomico di Cagliari, Via della Scienza 5, 09047, Selargius, CA, Italy

²⁸Department of Astronomy, Peking University, Beijing 100871, China

²⁹Cardiff Hub for Astrophysics Research and Technology, School of Physics and Astronomy, Cardiff University, Queen's Buildings, The Parade, Cardiff CF24 3AA, UK

³⁰Max Planck Institut für Astronomie, Königstuhl 17, D-69117 Heidelberg, Germany

³¹California Institute of Technology, Pasadena, CA 91125, USA; National Radio Astronomy Observatory, Pete V. Domenici Array Science Center, P.O. Box O, Socorro, NM 87801, USA

³²School of Physics, Peking University, Beijing 100871, China

³³Chinese Academy of Sciences South America Center for Astronomy, National Astronomical Observatories, CAS, Beijing 100101, China

³⁴Departamento de Astronomía, Universidad de Chile, Casilla 36-D, Santiago, Chile

ABSTRACT

We present the first $z = 0$ HI column density distribution function, $f(N_{\text{HI}})$, extending down to $\log(N_{\text{HI}}/\text{cm}^{-2}) = 17.8$. This was derived from high-sensitivity 21-cm emission-line imaging at ~ 1 kpc resolution. At high-column-densities ($19.8 < \log(N_{\text{HI}}/\text{cm}^{-2}) < 21.3$), our results align with earlier $z = 0$ studies but benefit from 100 times greater sensitivity. Comparisons with $z \sim 3$ quasar absorption-line studies reveal that $f(N_{\text{HI}})$ at $z = 0$ is systematically lower by 0.1-0.4 dex for $19.2 < \log(N_{\text{HI}}/\text{cm}^{-2}) < 21$. However, the distributions become comparable at $17.8 < \log(N_{\text{HI}}/\text{cm}^{-2}) < 19.2$, suggesting weak evolution in this regime. Extrapolating the length incidence (dN/dX) for $\log(N_{\text{HI}}/\text{cm}^{-2}) > 17.5$ implies a covering fraction (f_{cov}) of ~ 0.7 within 1-kpc-scale HI-detected pixels at $z = 0$. Notably, for $17.8 < \log(N_{\text{HI}}/\text{cm}^{-2}) < 20$, impact parameters at a given N_{HI} are significantly lower than previous $z \sim 0$ absorption-line results and TNG50 simulation predictions. This discrepancy indicates challenges in identifying galaxy counterparts for absorbers and in recovering low-column-density HI within cosmological simulations. Finally, we derive a covering fraction of 0.006 for $\log(N_{\text{HI}}/\text{cm}^{-2}) > 17.8$ gas within the virial radius around Milky-Way-like galaxies. These findings provide new constraints on the baryonic flows and gaseous dynamics governing galaxy evolution.

Keywords: Galaxy evolution, interstellar medium

1. INTRODUCTION

Galaxies need gas to form stars and grow. The atomic hydrogen, HI, is the major component of the interstellar medium (ISM) in star-forming galaxies, and serves as the reservoir of material for forming stars. Only high-column density ($\log(N_{\text{HI}}/\text{cm}^{-2}) \gtrsim 20.3$) HI in appropriate conditions can be efficiently converted to molecular gas and form stars (Bigiel et al. 2008, 2010). This high-column-density HI is almost exclusively found in the ISM, and contributes $\gtrsim 90\%$ of the cosmic HI mass (Zwaan et al. 2005b, Z05 hereafter). Yet, with a typical depletion time of 4 Gyr at $z = 0$ (Saintonge & Catinella 2022), and possibly even shorter at higher redshift (Walter et al. 2020), this high-column-density HI was not in the ISM from the beginning, and does not stay there forever in the lifetime of a galaxy. It is expected to be a dynamic reservoir, participating in the gas cycle of inflows, star formation and outflows (e.g., Crain et al. 2017). And it is the flow of gas traced by low-column density HI that has built and continuously replenishes this ISM reservoir (Péroux & Howk 2020).

Among the low-column densities, the range in N_{HI} between 10^{17} and 10^{20} cm^{-2} is possibly the most relevant and interesting in the gas accretion scenario. HI within this N_{HI} range is commonly referred to as LLSs (Lyman Limit Systems). QSO absorption at the Lyman limit has been the most important observational method over a wide range of redshifts. Observational developments make $z = 3$ the best redshift for LLS detections, though the situation is expected to improve with new instrumental efforts like the Blue-MUSE. At $z = 3$ both observations and simulations consistently suggest that LLSs are mostly in dark matter halos, and trace a large fraction of the inflowing gas, particularly the pristine one from the Inter-Galactic Medium (IGM) (Fumagalli et al. 2012; van de Voort et al. 2012). Gas traced by LLSs also includes static gas, outflowing gas, circulating gas, and tidally stripped gas, depicting a complex and dynamic picture of gas flows involving phase transitions (van de Voort et al. 2012). A statistical measure of the LLS HI distribution therefore

provides powerful constraints to the environment and driving physics of galaxy evolution.

The HI column density distribution metrics, including the distribution function, the incidence, the impact parameter, and the covering fraction, have helped develop macroscopic models and simulations of cosmological galaxy evolution (Ribaldo et al. 2011; Fumagalli et al. 2013, 2014; van de Voort et al. 2019), as well as recipes for sub-grid physical processes including feedbacks (Faucher-Giguère et al. 2016; Crain et al. 2017), microscopic gas hydrodynamic processes in the circum-galactic medium (CGM) (Ji et al. 2020; Stern et al. 2021) and radiative transfer involving the UV background (UVB) (Nagamine et al. 2010; Altay et al. 2011; Rahmati et al. 2013a; Yajima et al. 2012). Cosmological simulations reproduce the HI column density distribution function in the range 10^{17} to 10^{20} cm^{-2} at $z = 3$ reasonably well (van de Voort et al. 2012; Rahmati et al. 2015).

A major limitation with LLS observations is their restrictions to the QSO sight lines, making it impossible to contiguously map the gas distribution. The association of LLSs to host galaxies is complex, due to galaxy clustering (Qu et al. 2023; Weng et al. 2023), faintness of low-mass galaxies that contain a large fraction of the HI (Ribaldo et al. 2011; Lagos et al. 2014), and the dynamic nature of the multiphase gas (Chen et al. 2020). Finally, LLS observations struggle to collect sufficient statistics for a clear interpretation at $z = 0$ (Péroux et al. 2022). So far, no column density distribution function or length incidence for LLSs exist at $z = 0$. We cannot simply use the HI column density distributions observed at high- z (i.e. $z = 0.75$, the lowest redshift for LLS incidence length deviation in Fumagalli et al. 2013) to infer the one at $z = 0$, as the hydrodynamic and radiative environment of galaxies have evolved significantly since cosmic noon (Rahmati et al. 2013a; Faucher-Giguère 2020), in addition to the large-scale cosmic environment assembly. Around 20 years ago, 21-cm emission line imaging was used to derive the HI column density distribution function and related metrics for Damped Lyman α (DLA) like systems at $z = 0$ (Z05, Braun 2012; Ryan-Weber et al. 2003). Since then, the field has re-

mained relatively quiet, and no new measurements at $z = 0$ have been presented.

New radio telescopes recently made it possible to map the HI with around 1-kpc resolution down to the LLS column density regime. It is found that, down to a column density limit of $10^{17.7} \text{ cm}^{-2}$, the majority of detected HI is associated with dynamically cold galactic disks (Wang et al. 2024a; Yang et al. 2025), exhibiting no evidence of connecting to cosmic filaments except for temporary tidal tails (Lin et al. 2025; Marasco et al. 2025). The characteristic radius for the $0.01 M_{\odot} \text{ pc}^{-2}$ ($10^{18.1} \text{ cm}^{-2}$) surface density correlates tightly with the HI mass but not with stellar or dark matter halo mass (Wang et al. 2025). These new observations imply that the statistical HI column density distribution at $z = 0$ may differ from those at cosmic noon and earlier, where filamentary LLS structures may be prevalent (van de Voort et al. 2012).

The close association of $\gtrsim 10^{17.7} \text{ cm}^{-2}$ HI with galactic disks make it possible to count the cosmic column density distribution through weighting the galaxies according to the HI mass function (HIMF), a method firstly developed in Ryan-Weber et al. (2003) for the DLA-like N_{HI} . Contemporary developments in HI 21-cm statistical observations reveal that, the cosmic HI density, HIMF, and galactic HI mass fraction scaling relations have significantly evolved since $z = 1$ (Chowdhury et al. 2020, 2022a,b). Even since $z = 0.5$, the HI universe seems to have been actively evolving (Bera et al. 2022; Sinigaglia et al. 2022; Pan et al. 2023). It is therefore timely, feasible and necessary to revisit the cosmic HI column density distribution function and related metrics for the $z = 0$ universe, with column density limits 100 times deeper than 20 years ago, and the physical focus switching from the DLA-like HI near molecular gas and star formation locations, to the LLS-like HI extending toward and interacting with the CGM.

We use data from FEASTS (FAST Extended Atlas for Selected Targets Survey, Wang et al. 2023), and MHONGOOSE (MeerKAT HI Observations of Nearby Galactic Objects: Observing Southern Emitters, de Blok et al. 2024). These two surveys are the most sensitive 21-cm emission line imaging surveys at $z = 0$ at present for statistical samples. Section 2 provides more details about the data, as well as supplementary interferometric data from existing surveys and archives. These data are used to produce relatively uniform HI images with a column densities limit of $\sim 10^{17.8} \text{ cm}^{-2}$ at a resolution of 1 kpc in Section 3, which are then used to construct the HI column density distribution function ($f(N_{\text{HI}})$) in Section 4. Section 5 presents the main result, $f(N_{\text{HI}})$ derived to a $\log(N_{\text{HI}}/\text{cm}^{-2})$ limit of 17.8 at a resolution of 1 kpc for the $z = 0$ Universe. Section 6 compares the $z = 0$ $f(N_{\text{HI}})$ to those at high redshifts $z \geq 3$. The length incidences and impact parameter probability distribution at a given $\log(N_{\text{HI}}/\text{cm}^{-2})$ are also derived and compared to LLS results at $z = 0$ and $z = 3$ in section 6. We assume a Kroupa IMF (Kroupa 2001) in calculation of the stellar mass, and do not include helium in calculation of the HI mass. Throughout the paper we adopt the Λ CDM cosmology with the $\Omega_{\Lambda} = 0.7$, $\Omega_{\text{m}} = 0.3$, and $H_0 = 70 \text{ km s}^{-1} \text{ Mpc}^{-1}$.

2. DATA AND SAMPLE

2.1. The FAST images of FEASTS

FEASTS obtained HI images for 55 HI-richest Local-Volume galaxies that are above the Milky Way disk plane in FAST (Jiang et al. 2019, Five-hundred-meter Aperture Spherical radio Telescope) observable sky using on-the-fly mode, during the period 2021.09-2024.06.

The selection of FEASTS targets start from a master catalog of HI fluxes, combining the HI catalogs of Local-Volume galaxies, including the ALFALFA extended catalog (Hoffman et al. 2019), the catalog of Karachentsev et al. (2013), and the Hyperleda II catalog (Paturel et al. 2003). We select all the galaxies with HI flux $f_{\text{HI}} > 50 \text{ Jy km s}^{-1}$, corresponding to a predicted $R_1 > 3.3'$ according to the HI size-mass relation (Wang et al. 2016), where R_1 is the radius where the azimuthally averaged HI surface density reaches $1 M_{\odot} \text{ pc}^{-2}$ ($\sim 10^{20.1} \text{ cm}^{-2}$). Unperturbed HI disks should extend to $> 2R_1$ at the targeted detection $3\text{-}\sigma$ N_{HI} limit of $10^{17.7} \text{ cm}^{-2}$, based on the median HI radial profile of galaxies (Wang et al. 2025); perturbed HI disks can extend much further. We further select galaxies with $0^\circ < \delta < 60^\circ$ and Galactic latitude $|\text{b}| > 20^\circ$, and exclude M31 and M33 which are large galaxies in the Local Group. These selections result in a parent sample of 118 galaxies.

A subset of 44 galaxies with $f_{\text{HI}} > 100 \text{ Jy km s}^{-1}$ from the parent sample are taken as the high-priority sample and firstly observed. These galaxies have a predicted radii of $R_1 > 9.3'$, so can be relatively well resolved by FAST but may have serious short-spacing problems in previous interferometric observations. An additional random subset of 11 galaxies from the parent sample are also observed within the assigned time of the program. They are slightly less extended than the high-priority sample, but still well resolved in the diffuse, low-column density HI. We find only one galaxy, NGC 4192, whose emission is blended with the Milky Way cirrus. This cirrus was identified as large-scale ($\sim 0.5^\circ$) structures in HI emission detected in continuous channels between -77 and 41 km s^{-1} . NGC 4192 is therefore excluded, and the remaining observed sample of 54 galaxies are referred to as the observed FEASTS sample.

Each targeted galaxy in the observed FEASTS sample is mapped within a box region centered on the galaxy with a width L, where L is roughly the larger of 1° and $8 R_1$, but the shape is further adjusted (enlarged in the horizontal or vertical direction) using knowledge from previous HI interferometric or single-dish observations. Incidence of the radio frequency interference (RFI) contamination during the whole observation is minimal ($< 6\%$).

The observing mode, data reduction and source finding procedures are described in details in Wang et al. (2023, 2024a). We briefly summarize the key parameters and components here in the following. The data reduction pipeline includes standard modules of RFI flagging, calibration, gridding, and further spectral baseline flattening. The source finding procedure uses SoFiA (Serra et al. 2015; Westmeier et al. 2021), which identifies linked voxels above a thresh-

old of $4\text{-}\sigma$ after the cube is smoothed with a series of kernels that have a maximum size of 7 pixels ($210''$) in the x and y direction and 13 channels ($\sim 20\text{km s}^{-1}$) in the z direction.

The products include data cubes, source masks, and moment maps. The data cubes have a spatial resolution of $3.24''$ and a velocity resolution of 1.61 km s^{-1} . An error map is derived for each moment-0 image, with the value in each pixel calculated as $\sigma n_{\text{ch}}^{0.5} w_{\text{ch}}$ in unit of $\text{Jy beam}^{-1} \text{ km s}^{-1}$, where the σ is the cube rms in Jy beam^{-1} calculated as $3\text{-}\sigma$ clipped σ with voxels beyond the source masks, the n_{ch} the number of detected channels in the pixel line-of-sight, and w_{ch} the channel width in km s^{-1} . The moment-0 images are converted to the HI column density images, and the depth $N_{\text{HI,lim}}$ is estimated as the image contour level where the median $\text{S/N} = 3$. The median $N_{\text{HI,lim}}$ is $10^{17.71} \text{ cm}^{-2}$.

There are galaxies in interacting pairs or overlapping with small line-of-sight velocity differences. Using the procedure described in Wang et al. (2025) and Huang et al. (2025), we deblend the HI into different galaxies in 3D when possible, for the early-stage interacting systems and interlopers. The 3D deblending procedure takes optical positions and radio or optical velocities when available from the NED (NASA/IPAC Extragalactic Database), and use them as initial guess for positions of galaxies. It then utilizes the *watershed* algorithm in the 3D to segment a data cube into individual galaxies. As shown with mock tests in Huang et al. (2025), deblending in 3D is much more efficient and accurate in separating close galaxies than the traditional method in 2D. There it was also shown that pairs that have projected distances larger than their average R_1 and radial velocity difference larger than twice their average rotational velocities can be deblended with a flux accuracy of $> 90\%$. As in Z05, isolated HI clouds are assigned to closest galaxies.

2.2. The interferometric data to be combined with the FAST images of FEASTS

The FEASTS team have developed a series of tools to combine the FAST and interferometric HI data. The combined products effectively have the resolution of the interferometric data, and sensitivity close to that of the FAST data. This section introduces the interferometric data to be used for combination with the FEASTS data in this study.

2.2.1. HALOGAS

As the deepest interferometric HI survey in the northern sky, HALOGAS (Westerbork Hydrogen Accretion in Local GalaxieS, Heald et al. 2011) contributes data for 12 galaxies in the FEASTS sample. We take the high-resolution data cubes from the survey data release, which have a typical beam size of $20''$, channel width of 4.12 km s^{-1} , and cube rms of 0.2 mJy beam^{-1} . We do not use the much deeper low-resolution data cubes, so as to achieve similar physical resolution as other interferometry data collected in this study (see below).

2.2.2. THINGS

THINGS (The HI Nearby Galaxy Survey, Walter et al. 2008) has 13 galaxies in common with FEASTS, and three further in common with HALOGAS. The galaxy NGC4449 has an HI structure significantly exceeding the primary beam of VLA (FWHM $\sim 40''$), so we use alternative multi-pointing mosaics from the VLA archive (see below). We therefore use THINGS data for 9 galaxies. The survey data release shows that a natural-weighted data cube has typical beam size of 10 arcsec, channel width of 2.6 or 5.2 km s^{-1} , and cube rms of 0.4 Jy beam^{-1} . We use CASA (Common Astronomy Software Applications) to multi-scale clean the calibrated and continuum-subtracted THINGS visibilities largely following the same procedure as described in Wang et al. (2024a), but with an additional uv tapering of $10''$ and $20''$ for 5 and 4 galaxies, respectively. This additional uv tapering helps the final data set achieve relatively uniform depth and physical resolution (see section 2.4).

2.2.3. VIVA and LITTLE THINGS

The VIVA (VLA Imaging survey of Virgo galaxies in Atomic gas, Chung et al. 2009) and the LITTLE THINGS (Local Irregulars That Trace Luminosity Extremes, The HI Nearby Galaxy Survey, Hunter et al. 2012) each provide interferometric data for two galaxies. The survey data releases show that a typical VIVA natural-weighted data cube has a beam size, channel width, and rms of $20''$, 10.4 km s^{-1} , and 0.35 Jy beam^{-1} , and a typical LITTLE THINGS cube $10''$, 1.3 or 2.6 km s^{-1} , and 0.5 Jy beam^{-1} . We clean the calibrated and continuum-subtracted visibilities released by VIVA with a similar procedure as for THINGS, but without further uv tapering, as the resolution and sensitivity are already close to the target values. We take the natural weighted data cubes from the LITTLE THINGS data release. We do not clean the LITTLE THINGS data, as the multi-scale clean was already applied in the survey data release. Hunter et al. (2012) further conducted convergence tests to show that the residual fluxes are minimal after removing the convolved clean models from the dirty cubes.

2.2.4. Other VLA archival data

We obtain un-calibrated visibility data from the VLA archive for 16 galaxies. Among this subsample, two galaxies (NGC 4449 and NGC 3628) have multi-pointing observations so that extended structures can be relatively well mapped in a mosaic. These data are diverse in array configuration, observing time and RFI contaminating incidence, resulting in a relatively wide range of beam size and rms levels. We reduce them with a python pipeline built with CASA scripts following standard VLA 21-cm emission line data reduction procedures (Z. Liang et al. in prep). The clean procedure is similar to that described above for the surveys conducted at VLA.

2.2.5. The final FEASTS dataset

The interferometric datasets described above make the initial FAST+interferometry sample, which contains 45 galaxies. Figure 14 in Appendix summarizes the resolution and

N_{HI} sensitivity for all the interferometric data available from existing surveys or reduced by this team from the VLA archive. The column density sensitivity $N_{\text{HI,lim}}$ is estimated as the $3\text{-}\sigma$ limit assuming a line width of 20 km s^{-1} . The interferometric data for the seven galaxies that have resolution better than 0.8 kpc are degraded to 0.8 kpc resolution. The six galaxies with interferometric data resolution poorer than 2.4 kpc (an arbitrary criteria) are excluded from the initial FAST+interferometry sample. So the final FAST+interferometry sample (the *FEASTS sample* for short hereafter) has 40 galaxies. The $N_{\text{HI,lim}}$ is between $10^{18.6}$ and $10^{19.8} \text{ cm}^{-2}$. The $N_{\text{HI,lim}}$ and resolution for these 40 galaxies are further summarized in Table 2 in Appendix.

We use SoFiA to conduct source finding from these interferometric data cubes. We use the smooth-and-clip finder, and a series of smoothing kernels with maximum sizes equal to the beam major axis in the x and y directions, and the higher of $\sim 20 \text{ km s}^{-1}$ and 2 channels in the z direction. The smoothing kernels in the x and y direction are set to be relatively conservative, so to minimize the contamination of noise in the final moment maps.

2.3. MHONGOOSE

MHONGOOSE targets 30 nearby star-forming galaxies in the southern sky with MeerKAT (de Blok et al. 2024). The targeted galaxies have distances between 3 and 23 Mpc, and have been selected to have a relative uniform $\log M_{\text{HI}}$ distribution. The survey produces data cubes and moment maps for galaxies, at a series of different resolutions and column density sensitivities, ranging from $10^{17.8} \text{ cm}^{-2}$ at $90''$ resolution and $10^{19.7} \text{ cm}^{-2}$ at $7''$ resolution, for a line width of 20 km s^{-1} . At the distances of these galaxies, the resolution of $20''$ (the r10_t00 data) correspond to a physical resolution similar to that of the FEASTS+interferometry sample. The best column density sensitivity at $90''$ (the r10_t90 data) is very close to that of FEASTS.

2.4. The final main sample

The final main sample is the FEASTS sample of 40 galaxies plus the MHONGOOSE released sample of 30 galaxies, in total 70 galaxies. For the whole main sample, the galaxy distances are taken from the z0mgs ($z = 0$ Multiwavelength Galaxy Synthesis, Leroy et al. 2019). The star formation rate (SFR) and stellar mass (M_*) are taken from the z0mgs catalog and de Blok et al. (2024) for the FEASTS and MHONGOOSE sample, respectively.

The SFR, M_* and HI mass (M_{HI}) of the MHONGOOSE and FEASTS samples are displayed in Figure 1, with different symbols denoting the different samples of galaxies. The MHONGOOSE and FEASTS samples are dominated by dwarf and Milky-Way like galaxies respectively, but together they cover a relatively wide range of M_* and M_{HI} . MHONGOOSE is more evenly distributed in $\log M_{\text{HI}}$ range, but has relatively sparse sampling, particularly at the low and high- M_{HI} ends. FEASTS is biased toward the high- M_{HI} end, but helps fill M_{HI} bins throughout the whole M_{HI} range between $10^{7.5}$ and $10^{10.5} M_{\odot}$. These features can also be seen

from Figure 4-e. Both samples are biased toward highly star-forming and HI-rich galaxies, a bias to keep in mind.

3. PREPARING THE HI IMAGES

3.1. Combining FAST and interferometric data into full-HI images

We combine FAST and interferometric images into a single image, to achieve both high sensitivity and high resolution. All interferometric images used for combination have been corrected for primary beam attenuation. In each image, the interferometric data contribute the high-column-density and small-scale signals (referred to as the dense HI), while the initial FAST data only contribute the remaining diffuse HI that has intrinsically large scales. The large HI angular sizes for the diffuse HI are guaranteed by sample selection, and further supported by the characteristic radius r_{001} at a surface density of $0.01 M_{\odot} \text{ pc}^{-2}$ ($\sim 10^{18.1} \text{ cm}^{-2}$), being greater than $9'$, and 2.8-8 times the beam major axis (FWHM of PSF) in the FEASTS sample (Wang et al. 2025). When the diffuse HI has a large angular size that is well resolved by the FAST beam, the combined images are effectively the full-resolution HI images.

3.1.1. Preparations for combination

As the nature of the combination method is feathering, imaging artifact in the interferometric imaging data cannot be fixed and propagates to the creation of full-resolution column density map. To minimize this effect, all the interferometric cubes used in this study are visually inspected to ensure that there are no significant imaging artifacts.

As described in Wang et al. (2024a) and Wang et al. (2024b), the moment-0 images are used for the combination, to suppress systematic errors due to noise and unresolved structures in individual channel maps. From the interferometry side, moment-0 images derived from masked standard cubes (convolved clean models plus dirty residuals) are used when the data is from the HALOGAS or LITTLE THINGS, as these two datasets have high SNRs and relatively zero-level residuals. Otherwise, moment-0 images from the convolved models (without residuals being added) are used for combination, to avoid errors due to difference in clean and dirty beam areas (Wang et al. 2024a).

We cross-calibrate the flux levels between the FAST and interferometric images of each galaxy, using the procedure described in Wang et al. (2024a). In the flux cross-calibration procedure, the two types of data are compared in uv overlapping regions in the Fourier space, to derive the best-fit linear relation between them. The average factor for interferometric data to scale in order to match the FAST flux calibration is 1.04 ± 0.06 , consistent with typical radio flux calibration errors of 10%.

We also cross-calibrate the WCS systems of the two types of images, as described in Wang et al. (2024a). The WCS correction to the FAST image is determined as shifts in the WCS parameters CDELTA1 and CDELTA2 that lead to the lowest standard deviation in the difference image between the

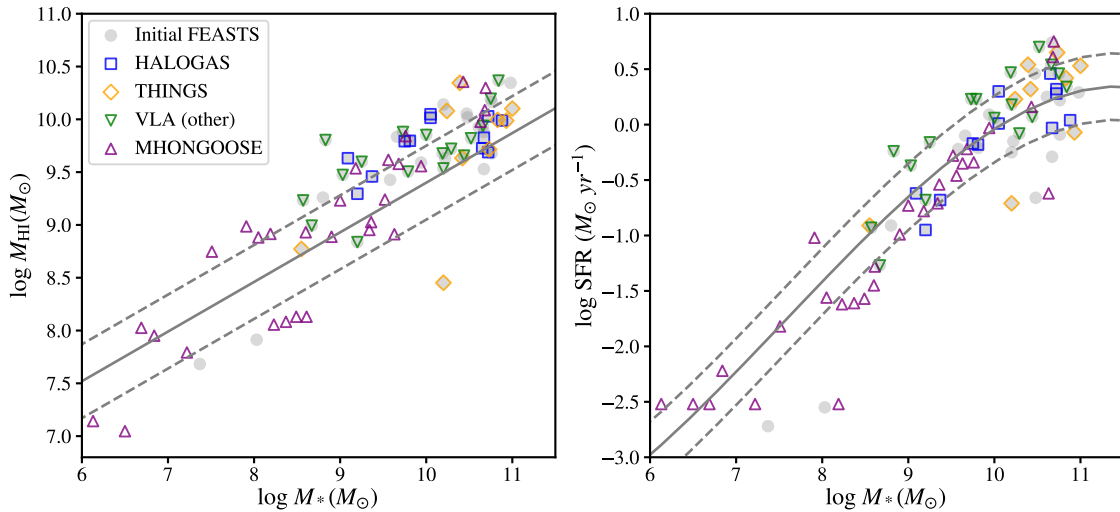


Figure 1. The location of the final sample in space of M_{HI} or SFR versus M_* . The solid and dashed lines in the left panel are for the star forming main sequence (SFMS) and scatter (Saintonge et al. 2016), and those in the right are for the median relation and scatter of galaxies on the SFMS (Catinella et al. 2018). The squares, diamonds, and downward triangles plot the FEASTS sample for which the interferometric data are taken from the HALOGAS, the THINGS and other VLA surveys or archive, respectively. The observed FEASTS sample of 55 galaxies are also plotted as grey dots for reference. The upward triangles plot the MHONGOOSE sample; one MHONGOOSE galaxy (J1321-31) has $M_* = 10^{4.7} M_\odot$ and $M_{\text{HI}} = 10^{7.6} M_\odot$, and is thus beyond the plotted range.

FAST and PSF matched interferometric images. The average WCS shift is around $8''$ in both x and y directions, consistent with the typical pointing error of $10''$ for FAST (Jiang et al. 2019).

In the next two sections, we use two different procedures, both of which can be classified as the linear method (Stanimirovic 2002), to combine the FEASTS and interferometric images.

3.1.2. The traditional combination procedure

The traditional procedure largely follows the workflow of Stanimirovic (2002) or IMMERGE of MIRIAD, and has been optimized for the FEASTS data to account for the average FAST beam shape in Wang et al. (2024b). The procedure transforms both images to the Fourier space, combines the two types of data with a weighting function, and then inverse-transform the combined data back to the image domain. The weighting function is solved by requiring the (FAST average beam + interferometric synthesized beam) combined beam to be equivalent to the interferometric synthesized beam. The inverse-transformed image is the final combined image.

Mathematically, what the procedure achieves is equivalent to convolving an interferometric image to have the PSF of the corresponding FEASTS image, obtaining the difference between the convolved interferometric image and FEASTS image (i.e., the diffuse HI), and adding this difference image back to the original interferometric image.

A possible problem associated with the first method is that the average beam is an imperfect representative of the FAST beams. The FAST imaging, like that of many other single-dish radio telescope utilizing multi-beam receivers, suffer

from variation of the multiple beams (Jiang et al. 2019; Chen et al. 2025), and non-Gaussian shape of the average beam due to light obscuration and refraction (Wang et al. 2023). These problems are most strong with the side-lobes of the FAST beams at the level of $\sim 5\%$ (Jiang et al. 2019; Wang et al. 2023; Chen et al. 2025), so they add systematic uncertainties to the low column densities, complicating interpretation of the faint HI structures. The problems are much mitigated after the traditional combination procedure, because the side-lobe effects are shifted to much lower column densities in a diffuse HI map than in a full HI map. But they cannot be ignored if the diffuse HI has a peak column density ~ 20 times higher than the image column density limit ($> 10^{19} \text{ cm}^{-2}$), which is often the case when combining with typical interferometric data (Wang et al. 2024a).

3.1.3. The new combination procedure

We design procedures to tackle the problems related to the imperfect average beam of FAST images. The goal is that, in the final full HI image, the diffuse HI is resolved with a uniform and clean (Gaussian) PSF with FWHM close to that of the FAST average beam obtained in Wang et al. (2023). The procedure has two crucial parts: accurate derivation of the diffuse HI, and beam correction for the diffuse HI.

In our previous work, the diffuse HI image is obtained by simply convolving the interferometric image with the FAST average beam, convolving the FAST image with the interferometric synthesized beam, and then subtracting the former from the latter (Wang et al. 2024a). Here, the interferometric image is effectively convolved in a different way, through the FAST observing simulator described in Yang et al. (2025).

The simulator mimics the tracking and response of each beam in the 19-beam receiver of FAST during real observation of the target, but uses the interferometric image as the mock sky. We then use the same pipeline that produces FAST HI images to grid the simulated observation into an HI image. The convolved FAST image minus the FAST-simulator processed interferometric image produces the diffuse HI image here.

High-quality FAST beam images are essential to perform the overall procedure described above. The beam images were taken during the FAST commissioning (Jiang et al. 2019), and have a dynamic range of 3.3 dex within a radius of $\sim 9'$ (Wang et al. 2023), sufficient for sampling the N_{HI} range from the FEASTS limit $10^{17.8}$ up to the “saturating” column density $10^{21.1} \text{ cm}^{-2}$, with the angular size $r_{001} > 9'$. For worst cases of edge-on ($i > 90^\circ$) galaxies that have high N_{HI} in the center and small angular sizes along the minor axis, Yang et al. (2025) showed that the N_{HI} minor-axis profiles measured from FEASTS images show clear excess over the average beam profile and its extrapolation, ensuring that no low- N_{HI} emission erroneously being introduced in (or taken away from) the diffuse HI images. Thus, on the whole, the FAST beam images plus the FEASTS HI images, in combination with the FAST observing simulator, allow relatively accurate extraction of the diffuse HI images.

Then, we only need to correct for the beam variation and non-Gaussian problems in the diffuse HI image. The corrected diffuse HI image plus the original interferometric image will produce the *full HI image*. We do not correct for the beam problems directly on the FAST images at an earlier step, because the systematic bias (and the uncertainty of correcting for them) due to an imperfect beam should be proportional to the surface brightness of the signals. Therefore, working on the diffuse HI images suppresses the uncertainties that would be introduced by image beam corrections.

In the following, we introduce the procedures that unify and clean the beam in the diffuse HI image.

- **Beam unification.** As demonstrated with mock tests in Appendix B, the beam variation problem is coupled with and amplified by the gridding process in image reduction, and shows up as sharp grid-like features in the final image. Therefore, it is possible to conduct “re-observation” to further amplify and separate these high-order features.

We use the original diffuse HI image as the mock sky for the FAST observing simulator, and produce the re-observed image. We subtract the re-observed image from the original diffuse HI image, and the resulting difference image serves as the correction image. Then, the correction image is subtracted from the original diffuse HI image. This corrected image has a beam similar to the average beam of FAST (Wang et al. 2023), and is taken as the beam unified image. The success of beam unification through this method is supported by mock tests in Appendix B.

- **Beam clean.** The original average beam deviates in shape from a 2D Gaussian function. Making the beam Gaussian-like is equivalent to the clean procedure commonly used in interferometric data reduction. We use the maximum likelihood method (Richardson 1972; Lucy 1974) to conduct the deconvolution, through a python script converted from its IDL version in IDL Astronomy User’s Library. We also tried the maximum entropy method (Agmon et al. 1979) with a python script converted from the same IDL library, but the results are less satisfactory and this method is not adopted in the end. Like the typical “clean” procedure, the residual image (input image minus the PSF-convolved model image) is derived in each iteration to assess the goodness of model.

We set $2\text{-}\sigma$ as threshold of convergency for peak residual fluxes within the detecting area of the input image, and 5000 as the maximum number of iterations. Convergence is typically reached within 5000 iterations. We visually inspect the final residual images to ensure the clean quality. The effectiveness of this beam clean procedure is also supported by the mock tests in Appendix B.

The mock tests in Appendix B also show that the diffuse HI surface density is reproduced with a relative uncertainty of $\lesssim 0.04$ dex.

3.1.4. The full-HI images of FEASTS

The full-HI images combined with the new procedure are used for main-stream analysis in this study. The main difference from the full-HI image produced with the traditional procedure is that the diffuse HI does not have significant beam variations throughout the image, or significant beam side lobes with respect to the Gaussian beam.

An example atlas of these full-HI images are displayed in Figure 2, in comparison to the interferometric and FAST-only images. The complete atlas can be found as supplementary material on-line. But we also compared to results obtained with the traditional combination procedure, as an estimate for the 19-beam systematic effects when the new procedure is not applied.

3.2. Constructing MHONGOOSE full-HI images

We combine the MHONGOOSE moment-0 images of different resolutions, in a way similar to the FEASTS+interferometric method. All the moment-0 images used have been corrected for primary beam attenuation, and are thresholded by requiring $S/N > 3$ before the following operation. The error images used to derive the SNR are obtained with the same procedure as in section 2.1.

The r10_t00 data has a similar angular and physical resolution as the interferometry dataset of FEASTS, and is taken as the highest-resolution signal in the combination. Starting from r10_t00 data, there are three types of data with successively lower resolution and higher sensitivity: r15_t00, r05_t60, and r10_t90. For each pair of successively two types,

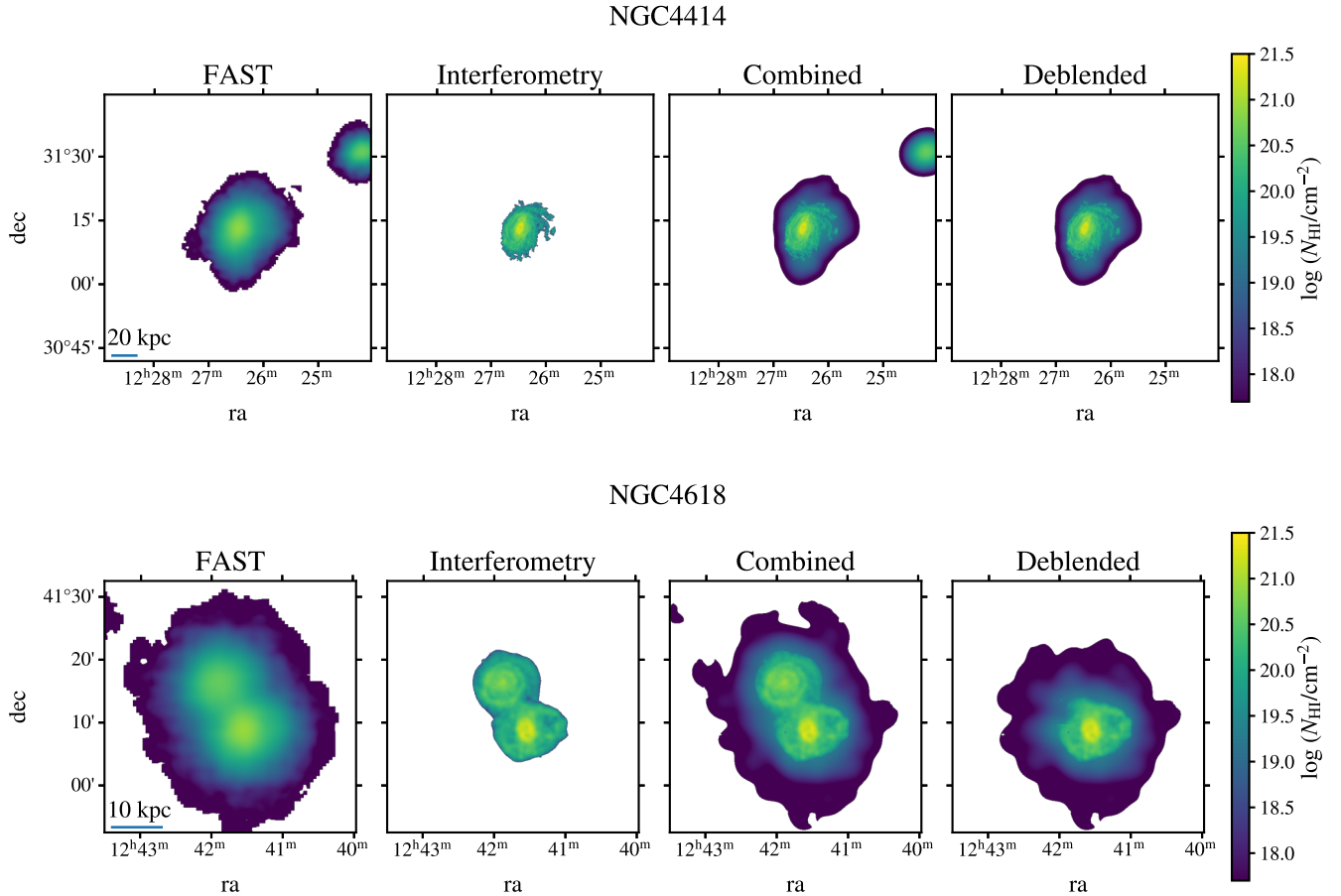


Figure 2. An atlas of column density maps for galaxies in the FEASTS sample. For each galaxy, from left to right, we display the column density maps from the FAST data, the interferometric data, the combined full-HI image, and the combined and deblended full-HI image, respectively.

we smooth the higher-resolution image to the resolution of the lower-resolution one, and subtract it from the latter. This difference image presents more diffuse signal uniquely detected in the lower-resolution image in the pair. In total, 3 difference images are derived for the 3 pairs of successive data types. They are all added to the highest-resolution image, which produces the full-HI image. The full-HI images have the resolution of the r10_t00 images ($\sim 10''$), and the $N_{\text{HI,lim}}$ of the r10_t90 images ($\sim 10^{18} \text{ cm}^{-2}$)

This procedure in principle is similar to the full-depth map construction introduced in de Blok et al. (2024). In de Blok et al. (2024), the full-depth maps are produced mainly to display in one plot the contour levels uniquely revealed in images of different sensitivities and resolutions. The main difference here from their method is that the contribution to low- N_{HI} regions of scattered light from high- N_{HI} regions is better accounted for. This approach may be sensitive to variations in the synthesised beam shapes which will range from Gaussian at high SNR to non-Gaussian at low SNR due to the deconvolution threshold. Because MeerKAT has a relatively flat noise level as a function of resolution, and

MHONGOOSE has relative conservative threshold in clean and source finding processes (de Blok et al. 2024), we assume this error to be relatively small. We present an example atlas of these MHONGOOSE full-HI images in Figure 3, in comparison to the original r10_t00 images.

4. CONSTRUCTING THE $F(N_{\text{HI}})$ TO $N_{\text{HI}} \sim 10^{17.8} \text{ cm}^{-2}$

In the following, we firstly summarize properties of the main sample (FEASTS+MHONGOOSE) and image data, to characterize the resolution and N_{HI} range of $f(N_{\text{HI}})$ to be constructed, and understand possible limitations. Then we explain the construction procedure for $f(N_{\text{HI}})$ (section 4.2). Finally, we discuss systematic uncertainties (section 4.3), and possible systematic dependence of $f(N_{\text{HI}})$ on sample and resolution, in light of comparison between studies (section 4.4).

4.1. Data quality in the context of $f(N_{\text{HI}})$ construction

Figure 4-a shows that, the median spatial resolution of the main-sample data is 1.2 kpc, and Figure 4-b shows that the 50 and 90-percentile of column density limit $N_{\text{HI,lim}}$ is $10^{17.8}$ and $10^{18.0} \text{ cm}^{-2}$. These statistics suggest that the $f(N_{\text{HI}})$

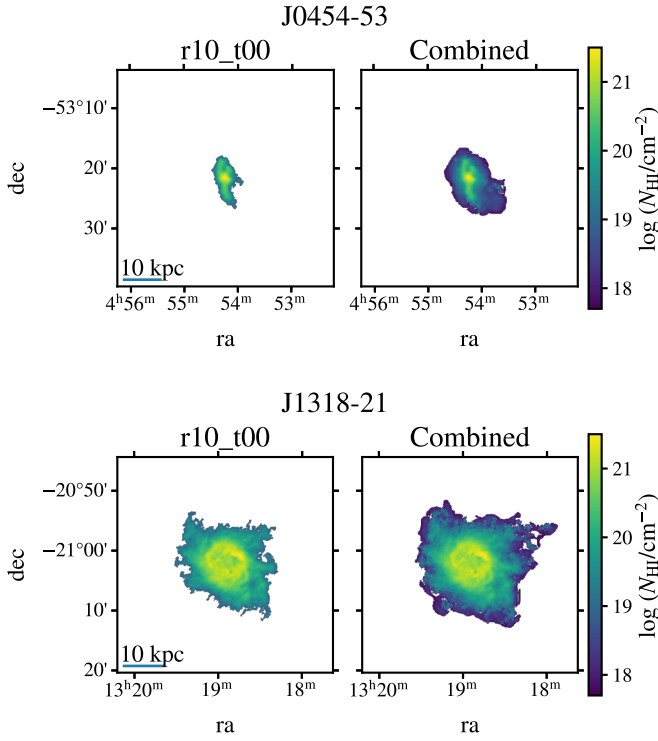


Figure 3. An atlas of column density maps for galaxies in the MHONGOOSE sample. For each galaxy, we display the column density maps from the r10.t00 data and the combined full-HI image.

constructed with the main sample is 50%-complete down to $10^{17.8} \text{ cm}^{-2}$ at ~ 1 -kpc resolution.

In order to accurately construct $f(N_{\text{HI}})$, the area counts of each N_{HI} should be statistically large, the images should spatially resolve the HI structures, the M_{HI} coverage of sample should be sufficiently wide and complete corresponding to the bulk of cosmic HI density according to the HIMF, and the inclination distribution should be relatively random ($\cos i$ following a uniform distribution) so to minimize biases caused by projection. With these considerations, Figure 4-c to d evaluate the feasibility of using the main sample images in constructing the $f(N_{\text{HI}})$.

Figures 4-c and d show the number of N_{HI} counts contributed by each galaxy with its available data above a column density level of 10^{18} cm^{-2} and 10^{20} cm^{-2} respectively. We have sufficient statistics putting the whole galaxy sample together for both $\log(N_{\text{HI}}/\text{cm}^{-2}) > 18$ and $\log(N_{\text{HI}}/\text{cm}^{-2}) > 20$. The $N_{\text{HI}} > 10^{18} \text{ cm}^{-2}$ areas are well resolved for individual galaxies throughout the main sample, with 10 and 90 percentiles of 245 and 1695 beams (Figures 4-c). The $N_{\text{HI}} > 10^{20} \text{ cm}^{-2}$ areas are also reasonably resolved in individual galaxies, with a minimum of 10 beams (Figures 4-d). On the other hand, the areas of $N_{\text{HI}} > 10^{21.3} \text{ cm}^{-2}$ are relatively poorly resolved, being sampled by < 30 beams in 23 galaxies (not plotted).

Figure 4-e shows that the M_{HI} ranges from 10^7 to $10^{10.7} M_{\odot}$, and we have at least one galaxy in each M_{HI} bin of 0.3 dex in the range $10^{7.5}$ to $10^{10.7} M_{\odot}$. The cosmic HI density contributed by the $10^{7.5}$ to $10^{10.7} M_{\odot}$ range can be estimated as $\sum_i \psi(M_i) \omega(M_i) M_i$ ¹. The result recovers 100.0% of the whole cosmic HI density Ω_{HI} reported in Guo et al. (2023), suggesting sufficient coverage in M_{HI} . The statistics seems overabundant at the high- M_{HI} end, but can be useful as the larger HI disks can be more perturbed and show larger variance between each other in N_{HI} histograms.

Figure 4-f shows that the $\cos i$ distribution is roughly flat. It is not perfectly uniform, but not strongly tilted toward 0 or unity, throughout the sample. Ensuring this rough flatness is important because more inclined galaxies tend to contribute more high- N_{HI} areas than low- N_{HI} ones due to projection.

To summarize, the main sample is sufficient for constructing a first $f(N_{\text{HI}})$ down to the $10^{17.8} \text{ cm}^{-2}$ level at a resolution of ~ 1 kpc. The relatively small main sample combined with galaxy diversity may cause systematic uncertainties, which may be worsened by the limited number of $\log(N_{\text{HI}}/\text{cm}^{-2}) > 21.3$ elements and limited number of high- i galaxies. We will thus quantify these uncertainties, together with uncertainties from distance errors and other factors, in section 4.3.

4.2. The $f(N_{\text{HI}})$ construction procedure

We largely follow the procedure of Z05 to construct the column density distribution $f(N_{\text{HI}})$ with the main sample.

The moment-0 images are converted to column density images with an optically thin assumption. The angular area of a column density image in each $\log(N_{\text{HI}}/\text{cm}^{-2})$ bin is counted, and the $\log(N_{\text{HI}}/\text{cm}^{-2})$ bins are set to range from 17.5 to 22.5 with a step of 0.1. The area (A_i) measured from each galaxy is assigned a weight proportional to the HIMF ψ_i evaluated at its HI mass (M_i), and inversely proportional to the number of galaxies in a $\log M_{\text{HI}}$ bin per the bin length (the $\omega(M_i)$). The $\log(M_{\text{HI}}/M_{\odot})$ bins are set to range from 7 to 10.7 with a size of 0.3. The $f(N_{\text{HI}})$ is calculated as

$$f(N_{\text{HI}}) = \frac{c}{H_0} \frac{\sum_i \psi(M_i) \omega(M_i) A_i (\log N_{\text{HI}})}{N_{\text{HI}} \ln 10 \Delta \log N_{\text{HI}}} \quad (1)$$

As in Z05, we calculate errors propagated from the HIMF parameters, and contributed by Poisson errors of area counts in each N_{HI} bin.

The major differences from the Z05 procedure are that

1. The reliable $\log(N_{\text{HI}}/\text{cm}^{-2})$ bins start from 17.8 instead of 19.8 (section 4.1).
2. The HIMF has been updated to the latest one constructed with the ALFALFA data (Guo et al. 2023). Because the new HIMF has much lower parameter errors than the one of Zwaan et al. (2003) used in Z05,

¹ For the i -th M_{HI} bin in the distribution, M_i , the ψ_i is the HIMF value at M_i , and the $\omega(M_i)$ is the reciprocal of galaxy number in the $\log M_{\text{HI}}$ bin per the bin length of 0.3 dex (see section 4.2)

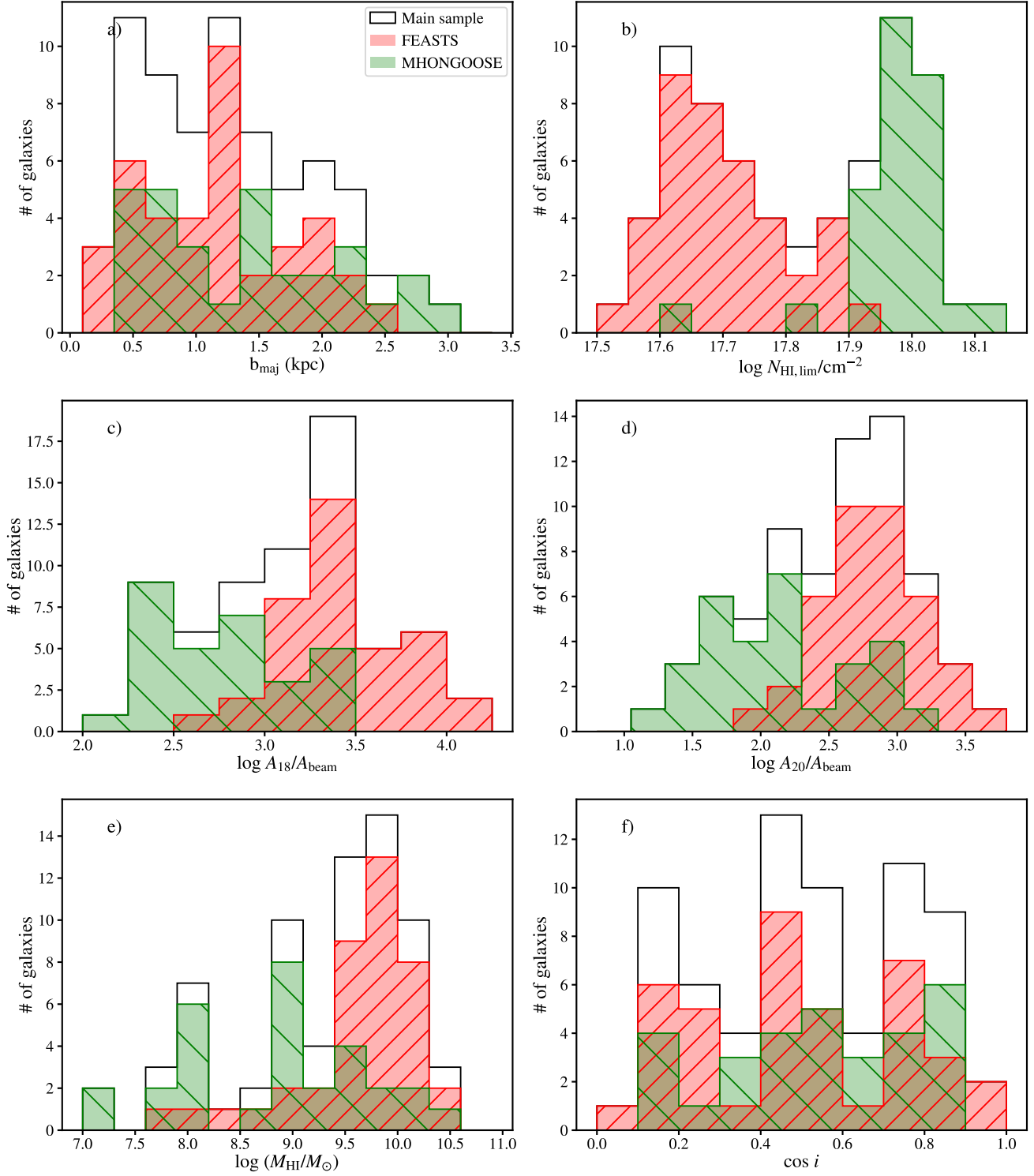


Figure 4. Properties of the main sample that are most relevant for $f(N_{\text{HI}})$ constructions. Panels a to f show the number distributions of galaxies in properties including image physical resolution (beam major axis in unit of kpc), image HI column density limit, the number of beam elements for $\log(N_{\text{HI}}/\text{cm}^{-2}) > 18$, the number of beam elements for $\log(N_{\text{HI}}/\text{cm}^{-2}) > 20$, the HI mass, and the galactic axis ratio. The distributions of the main sample (MS) are plotted as open histograms with black outlines. Distributions of the FEASTS sample are plotted in red histograms with upward diagonal stripes, and those of the MHONGOOSE sample in green histograms with downward diagonal stripes.

it propagates to much lower errors in the achieved $f(N_{\text{HI}})$.

3. The error bars additionally take into account the distance uncertainties and stochastic sampling of diverse galaxies. Consideration of these additional uncertainties is motivated by the sample properties discussed in section 4.1. As will be explained in section 4.3, these uncertainties contribute to $\gtrsim 80\%$ of the $f(N_{\text{HI}})$ variance throughout the N_{HI} range.

4.3. Systematic uncertainties

4.3.1. Systematic uncertainties due to distance errors and random sampling of diverse galaxies

We quantify systematic uncertainties in $f(N_{\text{HI}})$ that are caused by distance errors, stochastic sampling of galaxies in each $\log(N_{\text{HI}}/\text{cm}^{-2})$ bin, and stochastic sampling of high galaxy inclinations.

The distances of the main sample have a typical uncertainty of 30% (Kourkchi & Tully 2017; Leroy et al. 2019). We quantify the $f(N_{\text{HI}})$ uncertainty caused by this factor through randomly shifting the distances by an extent within $\pm 30\%$. We build 100 sets of such mock catalogs, repeat the $f(N_{\text{HI}})$ construction procedure for each set, and derive the standard deviations between these 100 sets of $f(N_{\text{HI}})$. These standard deviations are taken as systematic uncertainties associated with distance errors (green crosses in Figure 5-a). These uncertainties are around 0.02 dex when $\log(N_{\text{HI}}/\text{cm}^{-2}) < 21.3$, and become higher at the high- N_{HI} end. The high- N_{HI} areas tend to be in galaxy inner regions, are less self-similar or correlated in size with M_{HI} than the outer HI disks (Wang et al. 2025), and thus more sensitive to distances.

Quantifying the systematic uncertainty due to stochastic sampling of galaxies is motivated by the diverse HI morphology observed in and around galaxies (de Blok et al. 2024; Wang et al. 2024a). We derive the scatter of area counts as a function of N_{HI} in each M_{HI} bin that have more than six galaxies, and find values ranging from 0.2 to 0.4 dex. Such systematic differences between individual galaxies can contribute significantly to final errors, when the galaxy sample is not sufficiently large. We quantify the associated $f(N_{\text{HI}})$ uncertainty through bootstrapping the galaxies in each M_{HI} bin. In each bootstrapping round, for each M_{HI} bin with at least two galaxies, we resample the galaxies with replacement. Only the $M_{\text{HI}} \sim 10^{8.5} M_{\odot}$ bin has one galaxy and is excluded from this procedure. We repeat this procedure and produce 100 sets of resampled data, and derive $f(N_{\text{HI}})$ for each set. The standard deviations of $f(N_{\text{HI}})$ among these 100 deviations as a function of N_{HI} are the systematic uncertainties associated with stochastic sampling of galaxies in M_{HI} bins (blue dots in Figure 5-a). The typical uncertainties throughout the $\log(N_{\text{HI}}/\text{cm}^{-2})$ range of 18 to 21.3 are ~ 0.025 dex. They rise steeply at higher N_{HI} values where the area counts are small (section 4.1) and more prone to galaxy variations, reaching 0.25 dex at $\log(N_{\text{HI}}/\text{cm}^{-2}) = 22$.

The systematic uncertainty due to stochastic sampling of highly inclined galaxies is motivated by the fact that the $\log(N_{\text{HI}}/\text{cm}^{-2}) > 21.1$ areas primarily reflect projection effects. The deprojected HI surface densities rarely exceed $10^{21.1} \text{cm}^{-2}$, above which HI is efficiently converted to molecular gas (Bigiel et al. 2008). We evaluate the inclination associated systematic effects through bootstrapping the sub-sample with axis ratio below 0.3, corresponding to $i > 72^\circ$. These highly inclined galaxies are resampled with replacement, producing 100 data sets for calculating $f(N_{\text{HI}})$ scatters. The deviations (orange downward triangles in Figure 5-a) are only significant when $\log(N_{\text{HI}}/\text{cm}^{-2}) > 21.5$, and there they are close to those associated with stochastic samplings of galaxies in each $\log(N_{\text{HI}}/\text{cm}^{-2})$ bin (blue upward triangles). This deviation pattern confirms that the $f(N_{\text{HI}})$ at $\log(N_{\text{HI}}/\text{cm}^{-2}) > 21.1$ is mostly shaped by the high-inclination galaxies, and the errors there are dominated by stochastic sampling of these galaxies.

When we put the $f(N_{\text{HI}})$ errors together, Figure 5-b shows that, in the $\log(N_{\text{HI}}/\text{cm}^{-2})$ range between 17.8 and 21.3, the stochastic sampling of galaxies and distance errors dominate and contribute $> 80\%$ of the $f(N_{\text{HI}})$ variance in this study. The variance due to Poisson error of area counts contribute secondarily and only roughly 20% to the final variance. The contribution of HIMF errors are minimal in the final variance.

To sum up, when $17.8 < \log(N_{\text{HI}}/\text{cm}^{-2}) < 21.3$, $f(N_{\text{HI}})$ is relatively accurately determined, with errors less than 0.05 dex. When $\log(N_{\text{HI}}/\text{cm}^{-2}) > 21.3$, $f(N_{\text{HI}})$ is highly uncertain because the stochastic sampling is worsened by the even lower number of highly-inclined galaxies than the main sample.

4.3.2. Systematic uncertainties associated with the full-HI constructing procedure

We conduct mock tests to quantify possible errors related to the full-HI image construction (FAST+interferometry combination) for the FEASTS sample. Procedures producing the mock single-dish and interferometric image data are introduced in Appendix B. These mock data are processed and analyzed in the same way as for the real data. The mock measurements are compared with the true values as Mock(measure)–Mock(true) in Figure 6. The median systematic differences between the two are close to zero, suggesting that the fiducial full-HI image construction does not bring significant systematic biases to the $f(N_{\text{HI}})$. We therefore do not consider this type of errors in the $f(N_{\text{HI}})$ error calculation.

In Figure 6, we also evaluate the systematic differences in $f(N_{\text{HI}})$ between the old and new procedures of constructing FEASTS full-HI images (section 3.1). The $f(N_{\text{HI}})$ from the old procedure (FST(immg)) shows relatively small differences (< 0.05 dex) from that using the new and fiducial method (FST), when $\log(N_{\text{HI}}/\text{cm}^{-2}) > 18$. When $18 < \log(N_{\text{HI}}/\text{cm}^{-2}) < 18.8$, the differences are most apparent, approaching 0.1 dex. This type of error with the old imaging method will not decrease when the galaxy samples increase in the future. It is thus recommended to use the new proce-

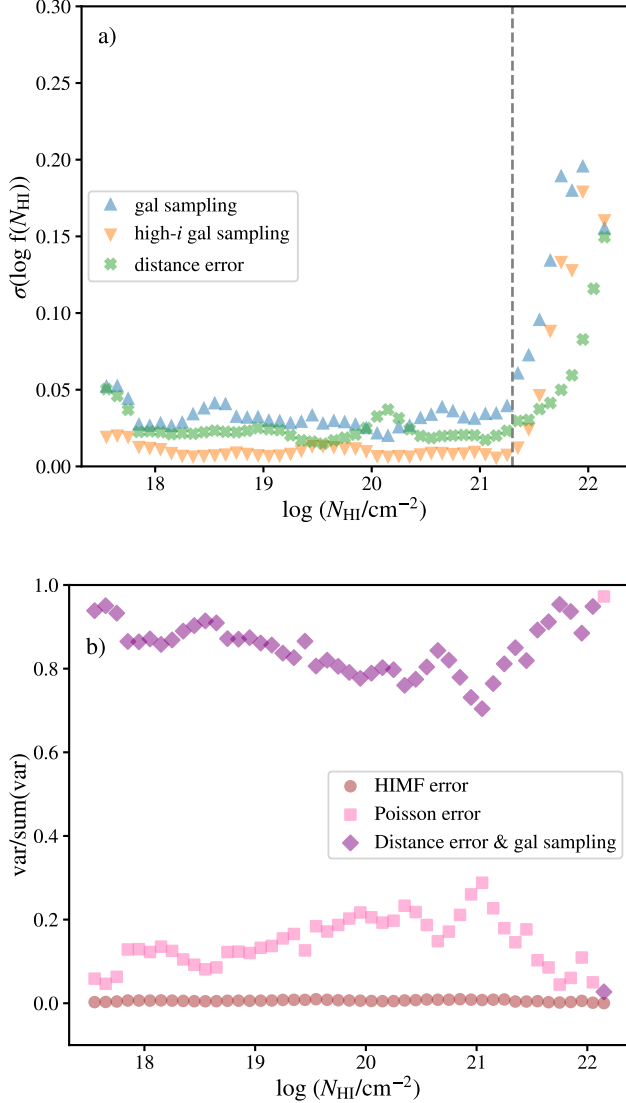


Figure 5. Systematic error estimation for $f(N_{\text{HI}})$. **Panel a:** different errors as a function of $\log(N_{\text{HI}}/\text{cm}^{-2})$. Three types of errors are considered, due to the stochastic sampling of galaxies (blue upward triangles), due to stochastic inclusion of highly inclined galaxies (orange downward triangles), and distance errors (green crosses). The vertical line marks $\log(N_{\text{HI}}/\text{cm}^{-2}) = 21.3$, above which the errors increase dramatically. **Panel b:** the contributions of different variance components to the final variance of $f(N_{\text{HI}})$. Three types of variances are considered: HIMF parameter error of Guo et al. (2023) (brown circles), Poisson error from the counts of $\log(N_{\text{HI}}/\text{cm}^{-2})$ areas (pink squares), and the combined effects of distance errors and galaxy stochastic samplings (purple diamonds).

dure to build the full-HI image, to reduce the errors as much as possible.

4.3.3. Systematic uncertainties associated with the optically thin assumption of HI

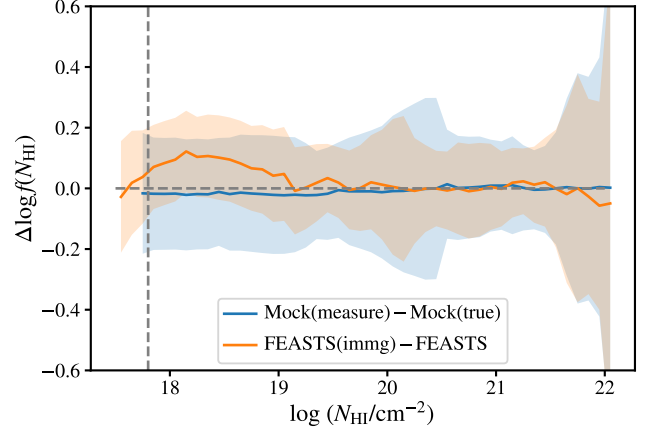


Figure 6. Systematical shifts of $f(N_{\text{HI}})$ due to different procedures of producing the full-HI images. Curves plot difference in $f(N_{\text{HI}})$ between full-HI mock images produced with different procedures. The $f(N_{\text{HI}})$ from images process with the fiducial procedure is compared with true answer: Mock(measure)-Mock(true). The $f(N_{\text{HI}})$ from FEASTS images processed with the old procedure is compared with that of the new method: FST(immg)-FST. The error bars are the propagation of $f(N_{\text{HI}})$ errors described in section 4, and not the scatters of offsets. The vertical dashed line marks the median limiting $\log(N_{\text{HI}}/\text{cm}^{-2})$ of 17.8.

We have assumed the HI to be optically thin when converting the moment 0 images to column density maps. As pointed out in Z05, the optically thin approximation may break down for the high- N_{HI} ($> 10^{21}\text{cm}^{-2}$) HI, leading to an underestimate of N_{HI} and artificial change in shape of $f(N_{\text{HI}})$ there (also see Braun 2012). But the effect should be insignificant for the remaining intermediate and low- N_{HI} regime, which is the main focus of this study. We estimate the systematic uncertainty associated with the optically thin assumption using the test below.

Previous studies have developed a “sandwich” model of the cool HI surrounded by two layers of warm HI, to explain the tight relationship between HI opacity and apparent N_{HI} , based on 21-cm emission and absorption observations of the Milky Way (Kanekar et al. 2011; Braun 2012). Adopting this model (Eq. 8 and 9 from Braun 2012), we correct for the HI self-absorption when calculating the column densities. The orange curve in Figure 7 shows that the difference of $\gtrsim 0.03$ dex between the corrected and direct N_{HI} , which is found to be 0.03 dex at a direct $\log(N_{\text{HI}}/\text{cm}^{-2})$ of 21, and leads to an offset of -0.025 dex in $f(N_{\text{HI}})$ at $\log(N_{\text{HI}}/\text{cm}^{-2}) = 21$. The differences in $f(N_{\text{HI}})$ between corrected and direct N_{HI} quickly drop to zero toward lower $\log(N_{\text{HI}}/\text{cm}^{-2})$, while they fluctuate around 0.1 with a large scatter due to poor statistics when $\log(N_{\text{HI}}/\text{cm}^{-2}) > 21$.

We thus conclude that for the $\log(N_{\text{HI}}/\text{cm}^{-2}) < 21$ regime, the HI self-absorption does not significantly affect our results. The cool and warm HI partition is still poorly constrained in external galaxies (see Pingel et al. 2024). Recent

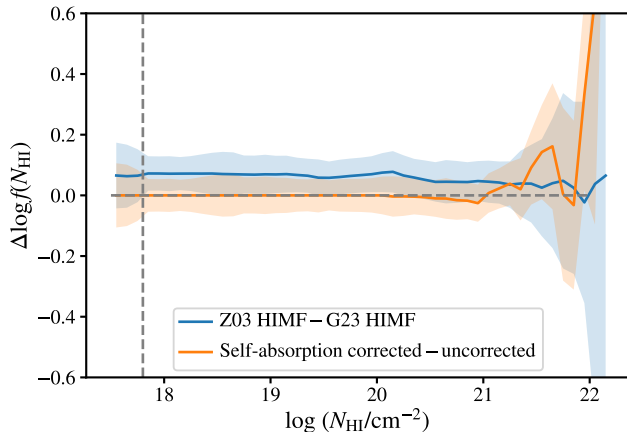


Figure 7. Systematical uncertainties of $f(N_{\text{HI}})$ related to 21-cm self-absorption and HIMF systematics. The blue curve plots the difference between assuming the Zwaan et al. (2003, Z03) HIMF and the fiducial Guo et al. (2023, G23) HIMF. The orange curve plots the difference between correcting and not correcting for self-absorption of the HI 21-cm emission line. The error bars (shaded areas) are the propagation of $f(N_{\text{HI}})$ errors described in section 4, and not the scatters of offsets. The vertical dashed line marks the median limiting $\log(N_{\text{HI}}/\text{cm}^{-2})$ of 17.8.

studies show evidence that some early conclusions on significant 21-cm self-absorption originated from blended and confused line-of-sight profiles, and that kinematically there is no strong evidence for optically thick HI throughout galactic disks (Koch et al. 2021). Therefore, we do not correct for this systematic offset due to self-absorption or add this uncertainty to the error bars of $f(N_{\text{HI}})$. Finally, the integral properties like cross-section, length incidence (see Section 6.2), and covering fraction (see Section 6.3) for $\log(N_{\text{HI}}/\text{cm}^{-2}) > 17.8$ should not be affected by the self-absorption.

4.3.4. Systematic uncertainties associated with different HIMF

The Guo et al. (2023) HIMF has been used because of its lower parameter error than the Zwaan et al. (2003) HIMF used in Z05. There is a systematic difference between HIMFs obtained from different datasets, reflecting systematic uncertainties because of data incompleteness and systematic dependence because of cosmic variance (Zwaan et al. 2005a; Ma et al. 2025). Specifically, Ma et al. (2025) showed that there is 0.2-0.3 dex difference in the high mass end of HIMF ($\log M_{\text{HI}}/M_{\odot} \geq 10$) between Zwaan et al. (2005a, updated HIMF based on Zwaan et al. (2003)) and Guo et al. (2023). Given that 13 out of 70 galaxies in the main sample have $\log M_{\text{HI}}/M_{\odot} \geq 10$, the systematic difference in HIMF at the high-mass end may contribute to the systematic errors in $f(N_{\text{HI}})$.

We evaluate this HIMF related uncertainty through deriving $f(N_{\text{HI}})$ with the Zwaan et al. (2003) HIMF, and compare the result to the fiducial one derived with the Guo et al. (2023) HIMF. The blue curve in Figure 7 shows that there is

an almost constant excess of 0.075 dex throughout the N_{HI} range in the former. Therefore, any offset of $f(N_{\text{HI}})$ between populations should be larger than 0.075 dex in order to be concluded physically robust against systematic uncertainties due to HIMF differences.

4.4. Additional systematic dependence

As a final step before presenting the derived $f(N_{\text{HI}})$, we discuss additional factors contributing to systematic shifts of $f(N_{\text{HI}})$, including different sample or data (FEASTS versus MHONGOOSE), and different spatial resolution. These two effects characterize possibly intrinsic dependence of the $f(N_{\text{HI}})$, but are not taken as errors.

For these quantifications of systematics, we derive a 0.3-kpc resolution $f(N_{\text{HI}})$ by constructing full-resolution MHONGOOSE images that start from the r00_t00 type (in contrast to the fiducial 1-kpc resolution measurements that are based on MHONGOOSE images starting from the r10_t00 type). We additionally construct 10-kpc resolution $f(N_{\text{HI}})$ for the main sample, using the deblended and cleaned FEASTS images without combining them with the interferometry data, and smoothing the MHONGOOSE r10_t90 images to the $3.24'$ angular resolution of FEASTS.

4.4.1. Sample dependence

For the systematics related to sample biases, we derive $f(N_{\text{HI}})$ for the MHONGOOSE and FEASTS sub-samples separately, and subtract from them the main-sample $f(N_{\text{HI}})$ so as to zoom in on the differences. Before looking into the difference, we note that, neither FEASTS nor MHONGOOSE have sufficient statistics to fill all the M_{HI} bins (Figure 4-e); it means that both $f(N_{\text{HI}})$ are lower limits due to the methodology of weighting galaxies by the HIMF $\psi(M_{\text{HI}})$. It also indicates that the main sample $f(N_{\text{HI}})$ does not necessarily lie between these two curves in all N_{HI} bins. So the difference quantified here should be viewed as upper limits to systematic differences due to sample biases or data differences.

In Figure 8-a, the FEASTS $f(N_{\text{HI}})$ is systematically higher than the MHONGOOSE $f(N_{\text{HI}})$ by 0.1 to 0.2 dex when $\log(N_{\text{HI}}/\text{cm}^{-2}) < 19.8$. A similar extent of differences is found when comparing the $f(N_{\text{HI}})$ measurements from the two datasets at a resolution of 10 kpc for $\log(N_{\text{HI}}/\text{cm}^{-2}) < 19$, implying that the former difference is not totally due to detailed difference in data capabilities of resolving intermediate-scale diffuse structures. At least part of the difference is likely a true sample difference, possibly related to different HI structures around low- (MHONGOOSE) and high-mass (FEASTS) galaxies, but the extent should on average be lower than 0.2 dex after removing possible upper-limit effects, which should be better quantified in the future after enlarging the samples.

4.4.2. Resolution dependence

Figure 8-b shows that the MHONGOOSE 0.3-kpc result differs little from the MHONGOOSE (1-kpc) one considering the error bars. The 1-kpc version only has a very small

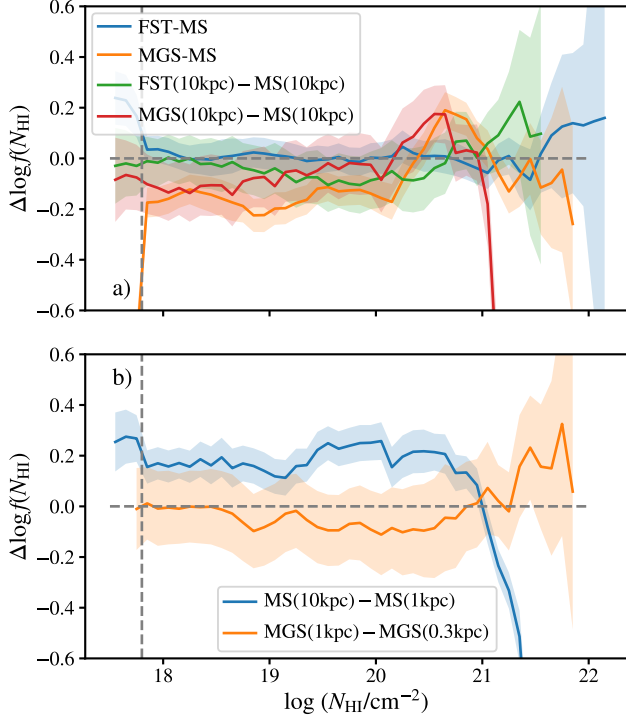


Figure 8. Systematical shifts of $f(N_{\text{HI}})$ due to different samples and resolutions. Curves plot difference in $f(N_{\text{HI}})$ between different datasets, with details in section 4.4. The vertical dashed lines mark the median limiting $\log(N_{\text{HI}}/\text{cm}^{-2})$ of 17.8. **Panel a:** differences in $f(N_{\text{HI}})$ between different samples with the same resolution. The main sample (MS), the FEASTS sample (FST), and the MHONGOOSE sample (MGS) are compared. In addition to the fiducial 1-kpc resolution (if not specified), $f(N_{\text{HI}})$ are also derived and compared at the 10-kpc resolution (denoted in the figure labels). **Panel b:** differences in $f(N_{\text{HI}})$ between the same sample with different resolutions. Three sets of resolutions are considered: 0.3 kpc (the MGS only), 1 kpc and 10 kpc.

difference with respect to the error bars from the 0.3-kpc version when $18.8 < \log(N_{\text{HI}}/\text{cm}^{-2}) < 21$. It indicates that at the 1-kpc resolution, the $f(N_{\text{HI}})$ can be relatively robustly derived for LLS-like systems.

In Figure 8-b, we find that the $f(N_{\text{HI}})$ of the main sample at the 10-kpc resolution is overestimated compared to that at the 1-kpc resolution by an almost constant excess of ~ 0.2 dex when $\log(N_{\text{HI}}/\text{cm}^{-2}) < 20.8$, compensated by significant under-estimates at higher N_{HI} . It suggests that between the 1-kpc and 10-kpc resolution, image smoothing tends to shift the $f(N_{\text{HI}})$ near the LLS regime upward in an almost parallel way. The shifting extent is not large compared to 1-kpc $f(N_{\text{HI}})$ error bars or MHONGOOSE versus FEASTS differences, both urging the need to increase 1-kpc-resolution sample size, and pointing to the potential of future lower-resolution observations in revealing distribution structures for the $\log(N_{\text{HI}}/\text{cm}^{-2}) \sim 18$ gas.

With the MHONGOOSE sample, we find a tentative contrary trend when increasing the 0.3-kpc resolution to the fiducial 1 kpc: some HI looks to be shifted from $18.5 < \log(N_{\text{HI}}/\text{cm}^{-2}) < 21$ to $\log(N_{\text{HI}}/\text{cm}^{-2}) > 21$. Because the $\log(N_{\text{HI}}/\text{cm}^{-2}) > 22$ HI in the 0.3-kpc images is smoothed out into the $21 < \log(N_{\text{HI}}/\text{cm}^{-2}) < 22$ range and disappears at the 1-kpc resolution.

These tests suggest that $f(N_{\text{HI}})$'s derived from different resolutions can have systematic differences of 0.1 to 0.2 dex, and the offset at a given N_{HI} is not necessarily a monotonic function of resolution, possibly a consequence of the intrinsic HI hierarchical structure. When the $f(N_{\text{HI}})$ is compared to that of the pencil-beam LLS observations, we should keep such systematic differences in mind.

5. RESULT: THE COLUMN DENSITY DISTRIBUTION

Figure 9-a shows the main result of this study, the $f(N_{\text{HI}})$ constructed from the main sample. The dashed vertical line marks the 50%-complete N_{HI} limit, below which $f(N_{\text{HI}})$ is less reliable.

Following the literature including Z05, we fit a Schechter function (Schechter 1976) to the $f(N_{\text{HI}})$ for the $\log(N_{\text{HI}}/\text{cm}^{-2})$ range of 17.8 to 22:

$$f(N_{\text{HI}}) = \frac{f^*}{N_{\text{HI}}^*} \left(\frac{N_{\text{HI}}}{N_{\text{HI}}^*} \right)^{-\beta} e^{-N_{\text{HI}}/N_{\text{HI}}^*} \quad (2)$$

The model thus consists of a power-law part for the low- $\log(N_{\text{HI}}/\text{cm}^{-2})$ regime with a logarithm slope of $-\beta$, and an exponentially declining part for the high- $\log(N_{\text{HI}}/\text{cm}^{-2})$ regime with a characteristic column density of N_{HI}^* . The Schechter function is commonly used to characterize galactic luminosity functions and mass functions (e.g., Zwaan et al. 2003; Guo et al. 2023).

The fitting is conducted in the logarithm space including the resolution-limited and uncertain $\log(N_{\text{HI}}/\text{cm}^{-2}) > 21.5$ side, mostly for capturing the total incidence of $\log(N_{\text{HI}}/\text{cm}^{-2}) > 18$. The likelihood function is assumed to be a simple Gaussian where the variance is underestimated by a fractional amount, f . The best-fit parameters (numerical optimum of likelihood function) are obtained with the `scipy.optimize` module. The posterior probability function and errors are estimated with the `emcee` (Foreman-Mackey et al. 2013) algorithm. Uniform distributions have been assumed, and ranges are set to be $(20.8, 22.6)$, $(0.8, 1.5)$, $(-2.5, -1)$ respectively for priors on $\log N_{\text{HI}}^*$, β , $\log f^*$, and $\log f$.

The best-fit parameters and errors are listed in Table 1. The standard deviation of data points around the best-fit model is 0.067 dex, and the data variance underestimation is lower than 0.01%. This model and the deviation from data points are also displayed in Figure 9-a. The `emcee` (Foreman-Mackey et al. 2013) generated corner figure can be found in Figure 17 in Appendix C. The figure shows that most projected posterior probability functions center on the best-fit values except for a negligible underestimate of $\log f$, and the covariance between parameters are relatively weak except for

Table 1. Parameters of the best-fit Schechter function

of $f(N_{\text{HI}})$.			
$\log(N_{\text{HI}}^*/\text{cm}^{-2})$	β	$\log f^*$	$\log f$
$21.26^{+0.02}_{-0.02}$	$1.150^{+0.016}_{-0.016}$	$1.754^{+0.036}_{-0.037}$	$-5.491^{0.128}_{-0.124}$

that between β and $\log f^*$. We do not show the parameter uncertainty associated model curve broadening, because it is very narrow.

When $\log(N_{\text{HI}}/\text{cm}^{-2}) < 17.8$, the measurement flattens compared to the best-fit model, most likely reflecting detection limit effects.

We compare our $f(N_{\text{HI}})$ results to the direct measurements and best-fit Schechter function of Z05 at $z = 0$ (Figure 9-b), which are based on data with a higher sensitivity limit of $\log(N_{\text{HI}}/\text{cm}^{-2}) > 19.8$ but similar spatial resolution as our data. Our $f(N_{\text{HI}})$ measurements are comparable with the Z05 Schechter function in the $19.0 < \log(N_{\text{HI}}/\text{cm}^{-2}) < 21.6$ range, but are ~ 0.2 dex lower than the Z05 measurements in the $20.2 < \log(N_{\text{HI}}/\text{cm}^{-2}) < 20.8$ range. Considering the HIMF difference (section 4.3.4), these two $f(N_{\text{HI}})$ measurements should be more consistent with each other if using the same HIMF. Therefore, in the $19.8 < \log(N_{\text{HI}}/\text{cm}^{-2}) < 21.6$ range, our $f(N_{\text{HI}})$ measurements are consistent with the Z05 results.

Our $f(N_{\text{HI}})$ measurements deviate from the Z05 extrapolation at low N_{HI} values. The deviation increases to around 0.3 dex at $\log(N_{\text{HI}}/\text{cm}^{-2}) = 18$, reflecting possible error amplification in extrapolation. At the highest column densities of $\log(N_{\text{HI}}/\text{cm}^{-2}) > 21.3$, our measurements also deviate from the Z05 curve, possibly due to high systematic uncertainties. Although the Z05 sample has a typical resolution (~ 1.3 kpc for their fiducial highest-angular-resolution dataset) similar to the main sample here (~ 1.2 kpc), small difference in the resolution distribution shape may also add to the $f(N_{\text{HI}})$ difference shown here.

In Figure 9-c, the $f(N_{\text{HI}})$ is also compared to the prediction of the cosmological simulation OWLS (Overwhelmingly Large Simulations, Schaye et al. 2010) in Rahmati et al. (2013a) (see also Rahmati et al. 2015 for the Evolution and Assembly of Galaxies and their Environment, EAGLE, simulation, Schaye et al. 2015) for $z = 0$. In that simulation, radiative transfer was performed in post-processing to account for ionizing UVB radiation and ionizing recombination radiation (Rahmati et al. 2013b). The Rahmati et al. (2013a) prediction roughly matches the $f(N_{\text{HI}})$ with offsets fluctuating around zero within the error bars when $\log N_{\text{HI}} < 20.2$. Particularly, the prediction seems to match perfectly the best-fit Schechter function in the same N_{HI} range, as can be seen from the similarity in residual shapes with respect to the direct measurements (top panels of Figure 9-c and 9-a). At higher N_{HI} , the Rahmati et al. (2013a) prediction can be less accurate, as pointed out by the authors, because ISM physics were treated in a relatively simple way there.

Studies using simulations to predict $f(N_{\text{HI}})$ or HI density distribution for the $\log(N_{\text{HI}}/\text{cm}^{-2}) > 17.2$ regime and

compare to observations have so far concentrated on the $z \sim 3$ slice of the Universe (Rahmati et al. 2013a, 2015; Villaescusa-Navarro et al. 2018; Sokoliuk et al. 2025). Previous simulation-observation comparisons for $z = 0$ instead focus more on reproducing the integral HI mass function and scaling relations, or distribution of $\log(N_{\text{HI}}/\text{cm}^{-2}) \gtrsim 20$ (Crain et al. 2017; Diemer et al. 2018; Davé et al. 2020). There are also simulation studies comparing $f(N_{\text{HI}})$ $z = 0$ predictions between recipes for the IGM at much lower N_{HI} or the ISM at the high- N_{HI} end (e.g., Crain et al. 2017; Tillman et al. 2023). Now it is possible to compare simulation and observation for the $\log(N_{\text{HI}}/\text{cm}^{-2}) > 17.8$ HI distribution. The observational $f(N_{\text{HI}})$ derived here for $z = 0$ (and related quantification in section 6.3 and section 6.2) provides a new anchor point for future simulation work.

6. DISCUSSION: RELATION WITH LLS COLUMN DENSITY FUNCTIONS, IMPACT PARAMETERS AND INCIDENCE

6.1. A modest decline of $f(N_{\text{HI}})$ since $z = 3$

We overplot in Figure 9-d, the $f(N_{\text{HI}})$ compiled by Zafar et al. (2013), with LLS, sub-DLA, and DLA observations at $z = 3$. They are based on data of SDSS (Sloan Digital Sky Survey) by Noterdaeme et al. (2012), UVES (Ultraviolet Visual Echelle Spectrograph) by Kim et al. (2002), and UVES by Zafar et al. (2013), respectively. The SDSS based result for $z > 3.3$ from Prochaska et al. (2010) is also plotted in Figure 9-d, which consists of 4 power law segments (thus more parameters than the Schechter function) fitted to their data in the N_{HI} range plotted here. We recall that the comparison is most robust for $\log(N_{\text{HI}}/\text{cm}^{-2}) < 21$, where the optically thin assumption works well (section 4.3.3).

The $z > 3.3$ $f(N_{\text{HI}})$ is almost always higher than the $z = 0$ one by $\gtrsim 0.2$ dex. For both $z > 3.3$ and $z = 3$, the large excess in $f(N_{\text{HI}})$ of $\log(N_{\text{HI}}/\text{cm}^{-2}) > 21$ should be lowered by a median of ~ 0.1 dex, if self-absorption is corrected in the $z = 0$ measurements. Systematics due to small sample size and self-absorption of the $z = 0$ $f(N_{\text{HI}})$ possibly produce the large fluctuation in $f(N_{\text{HI}})$ difference at $\log(N_{\text{HI}}/\text{cm}^{-2}) > 21$.

The $z = 3$ absorption based $f(N_{\text{HI}})$ is systematically higher than the $f(N_{\text{HI}})$ at $z = 0$ by an offset of 0.2 to 0.4 dex when $19.2 < \log(N_{\text{HI}}/\text{cm}^{-2}) < 21$. The differences become smaller toward lower $\log(N_{\text{HI}}/\text{cm}^{-2})$, with offsets 0.1–0.2 dex for $19.2 < \log(N_{\text{HI}}/\text{cm}^{-2}) < 20$, slightly larger than systematic uncertainties related to the HIMF variance. There is a hint for the offsets to disappear (< 0.1 dex) when $17.8 < \log(N_{\text{HI}}/\text{cm}^{-2}) < 19.2$, but the LLS sampling in $\log(N_{\text{HI}}/\text{cm}^{-2})$ also becomes much sparser.

The $z = 0$ result is at a resolution of around 1 kpc, while the covering fraction of HI clouds in a 1-kpc pixel, f_{cloud} , should be ≤ 1 . So the actual relative difference of the $z \gtrsim 3$ absorption-based measurements from the $z = 0$ ones needs be multiplied by a factor of $1/f_{\text{cloud}}$ (i.e., the offsets increasing by 0.16 dex if $f_{\text{cloud}} = 0.70$, more on this in section 6.2). Therefore, we conclude that it is possible for the $f(N_{\text{HI}})$ of LLS-like column densities to have declined slightly from $z = 3$ to $z = 0$. Such a modest evolution was not predicted in the

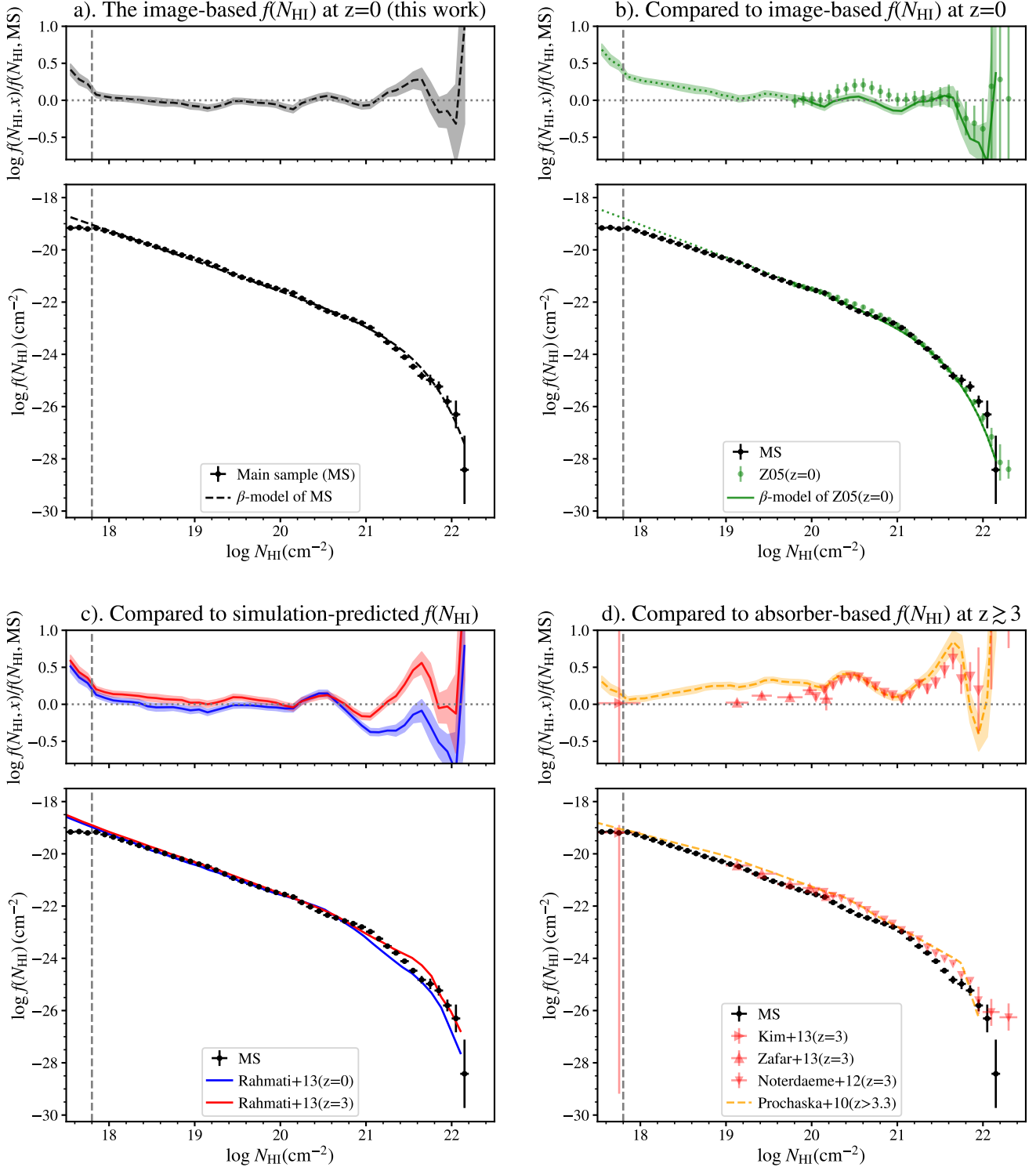


Figure 9. The HI column density distribution function $f(N_{\text{HI}})$ to the level of $10^{17.8} \text{ cm}^{-2}$ for $z = 0$, and its comparison to literature results. In each set, the lower panel shows the $f(N_{\text{HI}})$, and the upper panel the difference of best-fit models or literature results to the $f(N_{\text{HI}})$ derived in this study; the vertical dashed line mark the median $N_{\text{HI,lim}}$ of the main sample. **Panel a:** the direct derivation of $f(N_{\text{HI}})$ based on the main sample (MS) in this study is plotted as black dots and error bars. Its best-fit Schechter function is plotted as the purple curve. **Panel b:** comparing to the $f(N_{\text{HI}})$ of Z05, which is also derived from 21-cm emission line images but for $\log(N_{\text{HI}}/\text{cm}^{-2}) > 19.8$. The direct data points of Z05 are plotted as green dots, and its best-fit Schechter function is plotted as green solid and dotted curves when $\log(N_{\text{HI}}/\text{cm}^{-2}) > 19.8$ and < 19.8 respectively. **Panel c:** comparing to the simulation prediction from Rahmati et al. (2013a, OWLS) for $z = 0$ (blue curve), and $z = 3$ (red curve). **Panel d:** comparing to absorber-based $f(N_{\text{HI}})$ at higher redshifts. The absorption based measure of Kim et al. (2002, UVES), Zafar et al. (2013, UVES), and Noterdaeme et al. (2012, SDSS) for $z \sim 3$, are plotted in red rightward, upward, and downward triangles respectively. The absorption based piece-wise power law model of Prochaska et al. (2010, fit to SDSS observation) for $z > 3.3$ is plotted as a orange dashed curve.

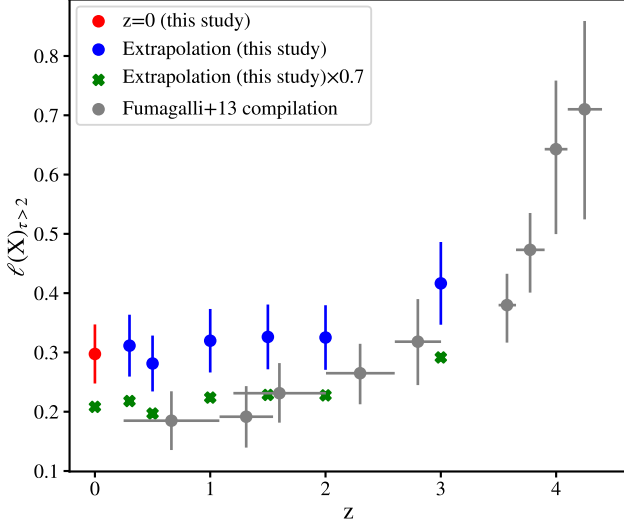


Figure 10. Length incidence for $\log(N_{\text{HI}}/\text{cm}^{-2}) > 17.5$ (optical depth $\tau > 2$). The red and blue dots are calculations based on $z = 0$ observations in this study. The direct $z = 0$ calculation (red dots) is based on cumulating the best-fit Schechter function of this study. The extrapolations (blue dots) are based on HI images in the main sample at $z = 0$, but HIMFs are the NUM predictions at different redshifts (Guo et al. 2023). The green 'X' symbols are the $z = 0$ direct and extrapolated calculations times a factor of 0.7 to guide the eye. The grey dots are LLS observations at different redshifts compiled by Fumagalli et al. (2013), from studies of Prochaska et al. (2010); Fumagalli et al. (2013); O’Meara et al. (2013); Ribaldo et al. (2011) for the redshifts range $z > 3.5$, $z \sim 3$, $1.5 < z < 2.5$, and $0.5 < z < 1.5$, respectively.

previous simulation OWLS (Rahmati et al. 2013a) as shown in Figure 9-c.

Although the UVB has declined by more than an order of magnitude since $z = 3$, previous studies have found that the evolution of $f(N_{\text{HI}})$ remains relatively modest for LLS, in contrast to the $3 < z < 6$ Universe where the LLS incidence drops quickly with decreasing redshift (Ribaldo et al. 2011; Fumagalli et al. 2013). This relatively modest evolution reflects a balance among several competing processes: the weaker UVB intensity tends to increase the neutral fraction, whereas collisional ionization in the increasingly hot CGM and the gradual decrease in the cosmic mean density act in the opposite direction. Feedback from star formation and active galactic nuclei further contributes by heating halo gas and enhancing collisional ionization, thereby lowering the neutral fraction and suppressing high- N_{HI} systems.

The partial cancellation among these radiative, thermal, and dynamical effects, together with continued structure growth and self-shielding in dense regions, helps preserve a broadly similar shape of $f(N_{\text{HI}})$ from $z \sim 3$ to the present. The systematic difference we observe between $z = 0$ and $z = 3$ thus captures the net outcome of these intertwined processes.

6.2. The length incidence

We relate the $f(N_{\text{HI}})$ measurements to length incidence (or line-of-sight density) of LLS absorbers at different redshifts.

For such comparison, we calculate the length incidence of, or reciprocal of mean free path between, absorbers with column density greater than N_{HI} , by

$$\ell(N_{\text{HI}}) = \frac{dN(N_{\text{HI}})}{dX}. \quad (3)$$

Here the number density, $dN(N_{\text{HI}})/dX$ for column densities larger than N_{HI} , is derived through integrating the $f(N_{\text{HI}})$ measurements or Schechter function: $dN(N_{\text{HI}})/dX = \int_{N_{\text{HI}}}^{10^{22.5}} f(N'_{\text{HI}}) dN'_{\text{HI}}$. It is related to the redshift number density $dN(N_{\text{HI}})/dz$ through: $\frac{dN(N_{\text{HI}})}{dX} = \frac{dN(N_{\text{HI}})}{dz} \frac{dz}{dX}$, where $dX = \frac{H_0}{H(z)} (1+z)^2 dz$. At $z = 0$, the $\ell(N_{\text{HI}}) = dN(N_{\text{HI}})/dz$, as $dz/dX = 1$.

Through integrating the directly measured $f(N_{\text{HI}})$ curve, we obtain $\ell(10^{17.8} \text{cm}^{-2}) = 0.267 \pm 0.033$. To better match the LLS column density range, we integrate the best-fit Schechter function, and obtain $\ell(10^{17.5} \text{cm}^{-2}) = 0.298 \pm 0.045$, where $\log(N_{\text{HI}}/\text{cm}^{-2}) \geq 17.5$ corresponds to an optical depth at the Lyman limit of $\tau \geq 2$. Through a similar calculation, we obtain $\ell(10^{17.2} \text{cm}^{-2}) = 0.345 \pm 0.052$, and $\ell(10^{17.8} \text{cm}^{-2}) = 0.256 \pm 0.039$. Fumagalli et al. (2013) pointed out that the varying results on ℓ in early studies could be partly due to inconsistent definition of minimum N_{HI} in the integration (Lanzetta et al. 1991; Storrie-Lombardi et al. 1994; Songaila & Cowie 2010). Our calculation above indicates an increase in $\ell(N_{\text{HI}})$ by a factor of 1.35 at $z = 0$ when the minimum N_{HI} decreases from $10^{17.8}$ to $10^{17.2} \text{cm}^{-2}$.

For reference, we also derive $\ell(10^{20.3} \text{cm}^{-2})$ for DLA-like systems, but warn that our sample size is not optimized for it. We obtain 0.037 ± 0.002 and 0.036 ± 0.002 with direct measurements and Schechter function respectively, both slightly lower than but roughly consistent with the value of 0.045 ± 0.006 derived in Z05.

6.2.1. The redshift dependence of LLS-like length incidence

The incidence rate can be understood as $\langle n\sigma \rangle$, i.e., the average of galaxy number density n times the HI cross section σ , where n is inferred by the ψ weighting in our $f(N_{\text{HI}})$ construction. At a resolution of 1 kpc, the incidence rate can be further expressed as 1-kpc resolution smoothed $\langle n\sigma \rangle_{1\text{-kpc}}$ times the surface cloud covering fraction f_{cloud} , where f_{cloud} is related to the 3D HI clumpiness, which is often described by the volume filling factor or clumping factor, and possibly linked to the turbulence (Suresh et al. 2019; Gronke & Oh 2020; Qu et al. 2025).

We can thus infer the evolution of LLS cross-section or covering fraction near $z = 0$ with the following experiment. We extrapolate the $f(N_{\text{HI}})$ at $z = 0$ to higher redshift by assuming that the HI distribution of each galaxy (equivalently, the N_{HI} distribution at a given M_{HI}) remains the same and only HIMF changes as a function of z . The HIMF of each z is predicted by the NeutralUniverseMachine (NUM, Guo

et al. 2023). We calculate the corresponding ℓ values of $\log(N_{\text{HI}}/\text{cm}^{-2}) > 17.5$, $\ell(10^{17.5} \text{cm}^{-2}) = \ell_{\tau > 2}$, and compare them to real LLS measurements in Figure 10. The extrapolated ℓ values are consistently higher than those at $0.5 < z < 3$ by a factor of 1.481 ± 0.212 .

This calculation of length incidence has extrapolated the Schechter function below the $\log N_{\text{HI,lim}}$ of 17.8 to 17.5, and there is a possibility of $f(N_{\text{HI}})$ flattening with respect to the Schechter function there. However, even if we force a flattening of the $f(N_{\text{HI}})$ to start at $\log(N_{\text{HI}}/\text{cm}^{-2}) = 17.8$, it only reduces the gap between the z -extrapolated and really observed ℓ at $z > 0.5$ by a factor of 16%. It is possible that NUM HIMF consistently over-estimates the HI galaxy densities at $z > 0$ by 1.481 times, but the Ω_{HI} through integrating the HIMF predicted by NUM matches the (Ly α -based) observations at different redshifts (Guo et al. 2023).

If the HIMF predictions of NUM is correct, then, either the $z = 0$ LLS-like HI has its $\langle n\sigma \rangle$ increased by a factor of 1.481 ± 0.212 compared to $0.5 < z < 3$, or the typical f_{cloud} is close to 0.675 ± 0.096 . While a larger $\langle n\sigma \rangle$ at $z = 0$ is possible as the UVB has declined by nearly 10 times since $z = 1$ (Faucher-Giguère 2020), the $f_{\text{cloud}} = 0.675 \pm 0.096$ of HI may be more likely, as recently studies on the low-temperature gas distribution and velocity structures suggest high level of turbulence (Chen et al. 2023).

The implied f_{cloud} seems comparable to the covering fraction of ~ 0.7 for strong Mg II absorbers at $z < 0.5$ out to 75 kpc around MW-like galaxies (Chen et al. 2010) (also see Kacprzak et al. 2008; Barton & Cooke 2009), or possibly larger than that of $f_{\text{cov}} \sim 0.1$ -0.65 for LLSs observed at $z \sim 3$ (Rudie et al. 2012; Prochaska et al. 2013b,a; Fumagalli et al. 2014). For the comparison with $z \sim 0$ ion absorbers, we note the possible difference in metallicities and hence possibly different structures. For a broader comparison with f_{cov} of LLSs in the literature, when the LLS searching radius (often the virial radius) is larger than where most LLSs locate, we expect $f_{\text{cloud}} > f_{\text{cov}}$.

6.3. Probability of detecting HI as a function of b and N_{HI}

We investigate the expansion of HI as a function of column density limits around associated galaxies. We derive cumulative probability distributions of impact parameter (or transverse distance) b around the galaxy center for HI with different column densities, $P(b)$. The $P(b)$ is constructed by weighting galaxy areas in the main sample HI images in a similar way as $f(N_{\text{HI}})$, but is cumulated and normalized to a total probability of unity in the parameter space. We compare $P(b)$ to distribution of data points from previous LLS observations at $z < 0.5$. The $z < 0.5$ LLS observations are from two data collections: one is from the MUSE-ALMA survey (Péroux et al. 2022) with the b derived in Weng et al. (2023), and the other is from Qu et al. (2025) (Z. Qu in prep). In both datasets, the lowest b (of the nearest possible host galaxy) is taken for the analysis here, when there is confusion for an absorber to be associated with multiple possible galaxies. So by construction, the LLS b would be biased toward low values, if the galaxy catalog were complete.

We firstly investigate the relative probabilities of detecting HI for a given b and N_{HI} . Figure 11-a shows the cumulative probability distribution of HI in the b versus $\log(N_{\text{HI}}/\text{cm}^{-2})$ plane. The accumulation starts from the highest probability density to the lowest one, so that 75% of HI in the plotted b versus $\log(N_{\text{HI}}/\text{cm}^{-2})$ range should be detected within the 0.75-level contour. A similar figure for DLA analogs can be found in Z05. In Figure 11-a, 95% of HI in the main sample is found with $\log(N_{\text{HI}}/\text{cm}^{-2}) < 19.2$, but less than one third LLSs are found there. The discrepancy implies that the absorber surveys of $\log(N_{\text{HI}}/\text{cm}^{-2}) > 17.8$ at low redshifts are biased toward DLA-like ones.

We then investigate the probabilities of locating the HI at transverse distances below b for a given detected N_{HI} . The probabilities of b are evaluated at a given N_{HI} , and accumulated starting from the smallest toward the largest b . So that 75% of the HI at a given $\log(N_{\text{HI}}/\text{cm}^{-2})$ should be detected at b lower than the 0.75-level line. Figure 11-b shows this cumulative conditional probability distribution of b given N_{HI} as a function of N_{HI} ; a similar figure for DLA analogs was presented in Z05. There is considerable discrepancy in Figure 11-b between 21-cm and LLS observations. The most striking one is that only 1 out of the 32 LLSs (+DLAs) are found within the 50% contour of cumulative b probability as a function of N_{HI} . The discrepancy is too large to be explained with the possible $f_{\text{cloud}} < 1$. Even if we assume an extremely small 10% covering fraction, and shift the LLS data points left-ward by 1 dex, only 4 out of 32 LLSs (+DLAs) would lie below the 50% cumulative probability curve.

This discrepancy could come from challenges in the LLS-galaxy pair identification, as pointed out in several recent studies (Chen et al. 2020; Weng et al. 2023). Absorber studies have difficulty in associating absorbers to galaxies because there can be satellites, other haloes along the line of sight or even denser gas from the IGM contaminating the association. A previous search in the TNG50 (Nelson et al. 2019; Pillepich et al. 2019) simulation found that the actual contribution to the HI from the central galaxy diminishes very quickly with increasing impact parameter (Weng et al. 2024). Observationally, there is evidence that these stronger absorbers tend to be found in galaxy over-densities (Péroux et al. 2022; Qu et al. 2023), implying that they are probing gas in more large-scale environments than the central galaxies or localized galaxy associations.

6.3.1. Comparing to the TNG50 predictions

We briefly compare the $f(N_{\text{HI}})$ and b probability distribution to TNG50 predictions for a subset of MW-like galaxies. Lin et al. (2025) conducted HI mock observations for 330 galaxies in the TNG50 simulation (Nelson et al. 2019; Pillepich et al. 2019) that are matched in M_* , M_{HI} , inclination, and distance to a sub-set of 33 Milky Way like galaxies selected by $M_* > 10^{9.5} M_{\odot}$ from FEASTS. The HI post-processing has been performed following contemporary standard procedures. The neutral gas fraction is determined differently in star-forming and non-star-forming cells, following the procedure of Diemer et al. (2018, see also Stevens et al.

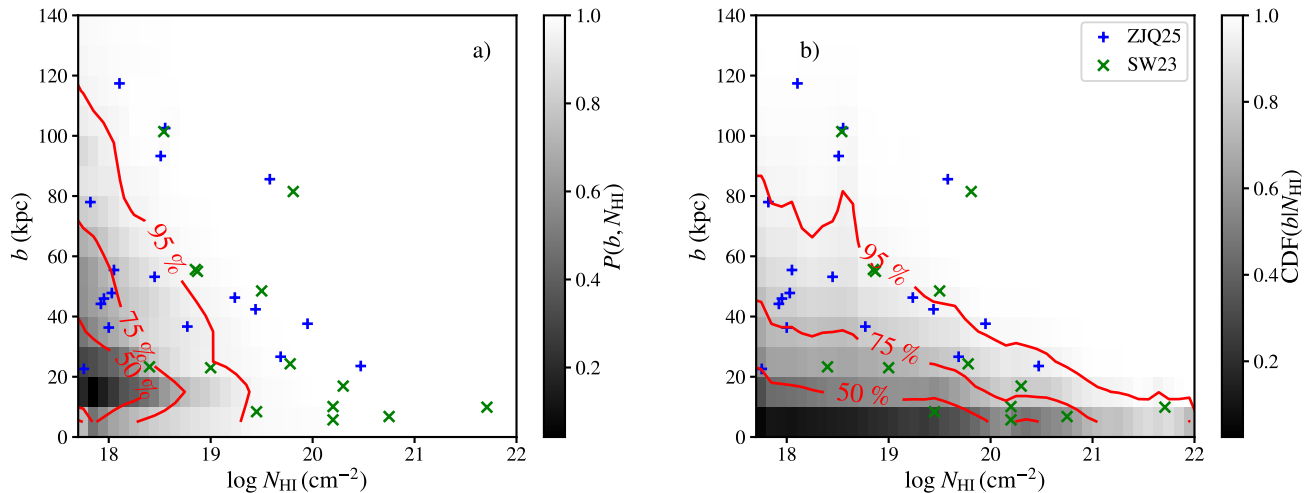


Figure 11. Probabilities of detecting HI in the space of N_{HI} and impact parameter b . **Panel a:** the colored map and associated contours show 2D cumulative probabilities of detecting HI in the space of impact parameter b versus $\log(N_{\text{HI}}/\text{cm}^{-2})$. **Panel b:** the colored map and associated contours show cumulative conditional probabilities of detecting HI below b as a function of N_{HI} . The probabilities are evaluated along different b for a given N_{HI} , and the accumulation starts from the smallest toward the largest b values

. In both panel a and b, the incidence of $z < 0$ LLSs from two low- z samples, Weng et al. (2023) (green x) and Qu et al. (2025) (blue +), are plotted for comparison.

2019). The HI-H₂ partition follows the procedure of Marinacci et al. (2017), using the model of Leroy et al. (2008). The total HI masses obtained for mock galaxies are consistent with the TNG50 catalog of Diemer et al. (2018) with an offset of 0.038 ± 0.028 dex.

The mock images are deblended with the same procedure as for the observational data of this paper. There are 23 of the 33 galaxies in that sub-set included in the main sample. We compare the measurements from the property-matched TNG50 mocks at a resolution of ~ 1 -kpc matched to these 23 FEASTS galaxies.

Figure 12-a compares the $f(N_{\text{HI}})$, and Figure 12-b and Figure 12-c compare the b probabilities. They are plotted in similar way to those in Figures 8 and 11, but for MW-like galaxies from the FEASTS sample. Although the TNG50 predicted $f(N_{\text{HI}})$ is similar to the observational one (with median offset being 0.03 ± 0.03 when $17.8 < \log(N_{\text{HI}}/\text{cm}^{-2}) < 21.3$), its predicted impact parameters are too large when $\log(N_{\text{HI}}/\text{cm}^{-2}) < 20$. For a given $\log(N_{\text{HI}}/\text{cm}^{-2}) < 19$, only 75% of the predicted HI is found within the 95-percentile b of the observed HI, and the most extended 25% of the predicted HI has b larger by 30-50% than that of the observed HI.

Lin et al. (2025) find that TNG50 over-predicts HI radius at the $\log(N_{\text{HI}}/\text{cm}^{-2}) \sim 18$ level when galaxies are massive or having low HI mass fractions within the MW-like sample (also see Marasco et al. 2025). Here, through the HIMF-based weighting, the b probabilities have more contributions from slightly less massive galaxies than the initial MW-like subsample of FEASTS. Yet, significant differences

are still observed in the b probability distributions². Such a difference can be a mixed problem of unrealistic cool gas ($> 10^4$ K) distribution in TNG50, and imperfect HI postprocessing.

The comparisons here suggest that the conditional b probability distributions at a given N_{HI} can be very useful constraints to cosmological simulations.

6.3.2. The N_{HI} versus b relations

We investigate the probabilities of locating HI at b for a given detected N_{HI} . Figure 13 plots the relevant cumulative conditional probability distribution of b given N_{HI} , as a function of N_{HI} , with b normalized by different units. The probabilities are evaluated along b for a given N_{HI} , and the accumulation starts from the highest probability density toward lower values. The radial units considered include the physical kpc, r_{200} , r_{001} , and r_{18} .

The dark matter halo virial radius r_{200} are estimated from the stellar mass of associated galaxies using the stellar mass-halo mass relation of Behroozi et al. (2019), with a uncertainty of ~ 0.1 dex. This simple estimation does not consider galaxy clustering or central versus satellite differences, and implies focus on the localized halo that is assumed to be relatively unperturbed and constrains the HI disk. The r_{001} is the radius at a projection-corrected and azimuthally averaged surface density level of $0.01 M_{\odot} \text{pc}^{-2}$ ($10^{18.1} \text{cm}^{-2}$). The r_{18} is the radius at an azimuthally averaged column den-

² We also tried comparing the covering fraction of HI at the 1-kpc resolution as a function of galaxy centric radius. The difference between TNG50 prediction and observation is less significant than the b comparison.

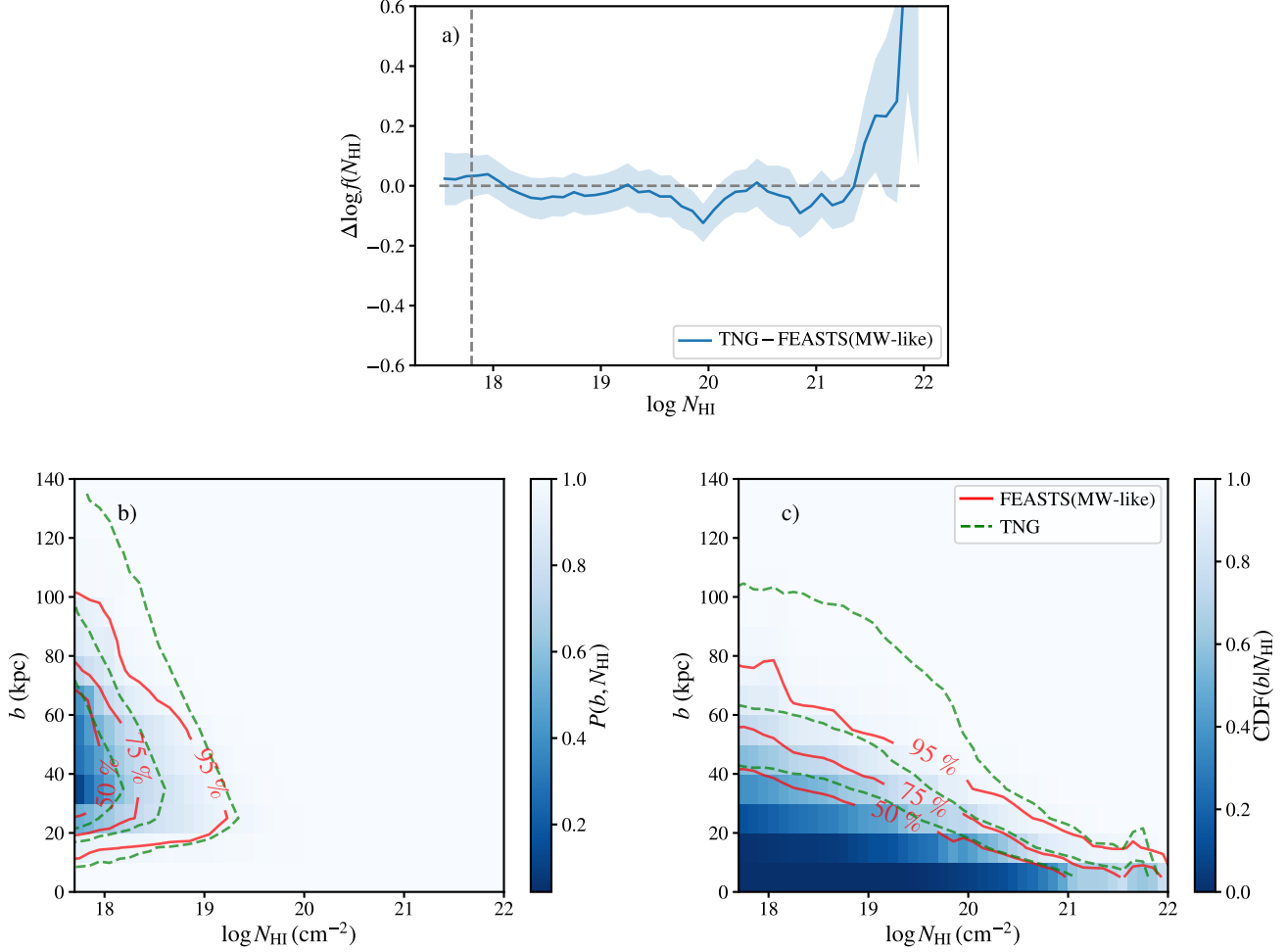


Figure 12. Panel a: the offsets in $f(N_{\text{HI}})$ between TNG50 predictions and observations for MW-like galaxies. The MW-like galaxies are selected from the FEASTS sample, and the TNG50 sample is a property matched control sample for the FEASTS sample (Lin et al. 2025). **Panels b and c:** probabilities of HI detections in the 2D space of N_{HI} and impact parameter b . Similar to Figure 11, but comparing the observation and the TNG50 simulation, and only for MW-like galaxies from FEASTS (red solid contours) and their control sample from the TNG50 (green dashed contours).

sity of 10^{18} cm^{-2} without projection correction. Because azimuthal averaging involves areas with $\log(N_{\text{HI}}/\text{cm}^{-2})$ both below and above 18, the r_{18} does not necessarily represent the average galactocentric radius to find $\log(N_{\text{HI}}/\text{cm}^{-2}) = 18$ pixels.

In Figure 13, the tightest $P(b)$ distribution (lowest relative scatter) is found when the normalization is with r_{001} and r_{18} . At $\log(N_{\text{HI}}/\text{cm}^{-2}) = 17.8$, the median b in normalization of kpc, r_{200} , r_{001} , and r_{18} is 30, 0.17, 0.85, and 0.82, respectively. The $1-\sigma$ relative scatter derived as half width between the 0.68 contours are 60, 43, 20 and 20%, respectively. The scatter of b/r_{200} is much larger than could be produced by uncertainties of r_{200} . There seems to be a bimodality in the b/r_{200} distribution near $\log(N_{\text{HI}}/\text{cm}^{-2}) = 18$, which is possibly a result of complex sample selection and will not be discussed here.

The median $b/r_{001} - \log N_{\text{HI}}$ relation for $\log(N_{\text{HI}}/\text{cm}^{-2}) < 20.5$ is:

$$b/r_{001} = \log(N_{\text{HI}}/\text{cm}^{-2}) \times (-0.19 \pm 0.01) + (4.26 \pm 0.25). \quad (4)$$

Therefore, if the optical counterpart identification is secure, one can use the following procedure to estimate the M_{HI} for each LLS associated galaxy with observed N_{HI} and b .

1. Using the N_{HI} value to infer the b/r_{001} from the median relation in Figure 13-c.
2. Combining with the observed b to derive r_{001} .
3. Estimating M_{HI} with r_{001} based on the $r_{001}-M_{\text{HI}}$ relation (Wang et al. 2025).

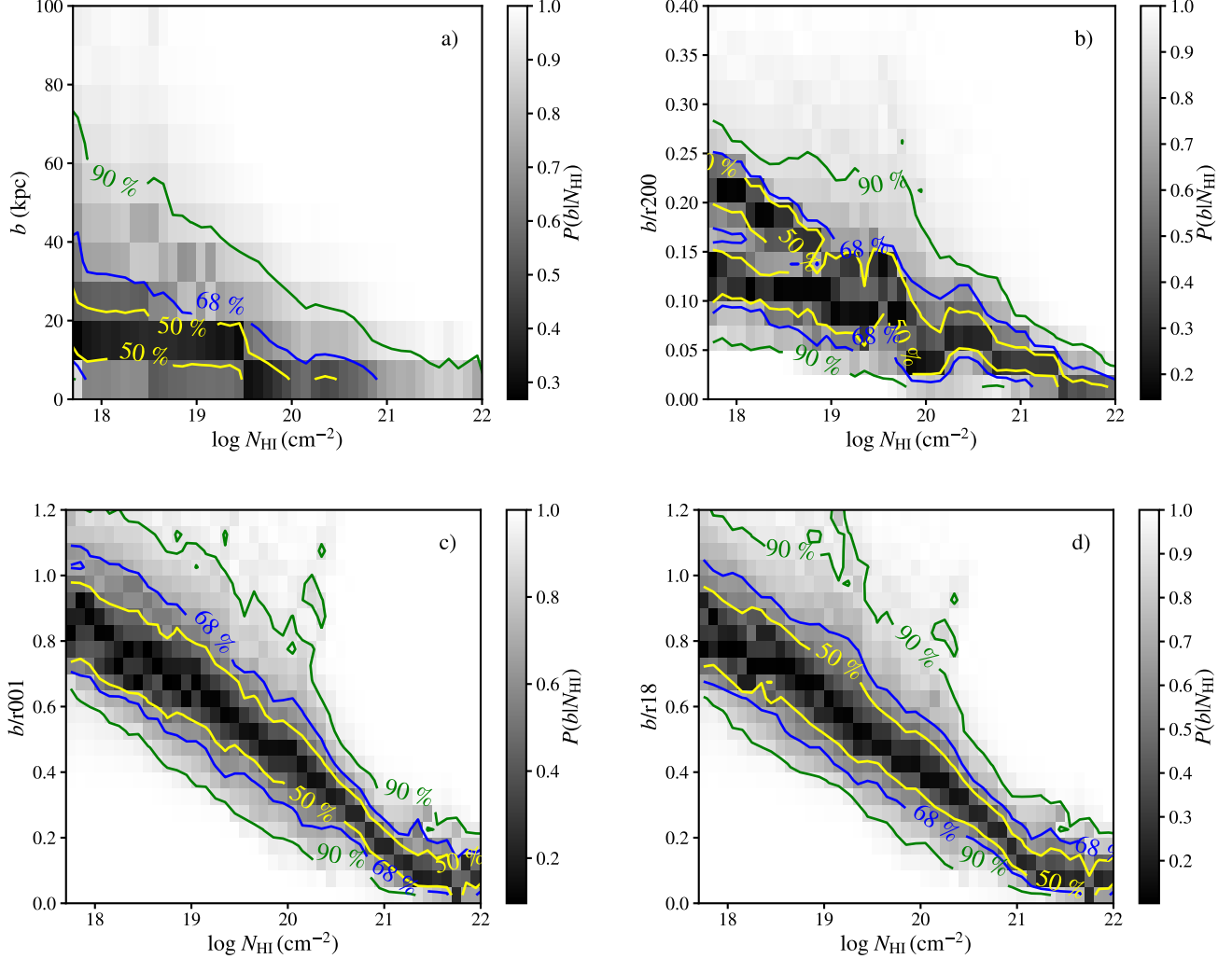


Figure 13. Cumulative conditional probabilities of impact parameters b given N_{HI} , as a function of N_{HI} in different normalizations of b

. The probabilities are evaluated along b for a given N_{HI} , and the accumulation starts from the highest probability density toward the lower ones. From panel a to c, the normalizations used are the physical unit kpc, the virial radius r_{200} , the $0.01 M_{\odot} \text{pc}^{-2}$ -HI radius r_{001} , and the 10^{18}cm^{-2} -HI radius r_{18} , respectively. The green, blue and yellow contours show the 90, 68 and 50% probabilities.

The $1\text{-}\sigma$ uncertainty of this estimate is 0.12 dex, considering both the scatter of b/r_{001} at a given N_{HI} , and the scatter of M_{HI} around the size-mass relation.

6.3.3. HI covering fraction around MW-like galaxies

The covering fraction of HI above a certain N_{HI} within the virial radius of dark matter halos, f_{cov} , has been commonly adopted in parametrizing HI distribution both in observations and in simulations (Prochaska et al. 2013b; Fumagalli et al. 2014; Rahmati et al. 2015; Faucher-Giguère et al. 2016; Tortora et al. 2024). Because the N_{HI} profiles align best with r_{001} that strongly correlates with the M_{HI} (Wang et al. 2025), the f_{cov} of LLSs should strongly depend on the HI mass fraction of the central galaxy. Therefore, comparisons of f_{cov} should only be conducted between samples with matched HI richness.

Former cosmological simulations predicted f_{cov} that was too low compared to observations at $z = 3$. This has been largely alleviated through increasing resolution and adjusting stellar feedback recipes (Faucher-Giguère et al. 2015, 2016; Rahmati et al. 2015; van de Voort et al. 2019). Modern cosmological simulations usually fail to find a correlation of f_{cov} with the halo mass, and predict very low f_{cov} at large galactic distances for MW-like halos at $z \sim 0$ (Tortora et al. 2024).

Our result that the N_{HI} radial profile is mostly determined by M_{HI} supports the lack of correlation of f_{cov} with halo mass at $z = 0$. It also hints at the possibility for a relatively low f_{cov} within the virial radius at $z \sim 0$, because the general galaxy population for a halo-mass-selected MW-like sample should be relatively gas poor. The median $\log M_{\text{HI}}/M_{*}$ of FEASTS MW-like galaxies that have $M_{*} \sim 10^{10.5} M_{\odot}$ is ~ -0.5 (Figure 1), 0.8 dex higher than that of a general galaxy with

the same M_* (Saintonge & Catinella 2022). Through the HI r_{001} - M_{HI} relation (Wang et al. 2025) and the b/r_{100} - N_{HI} relation (equation 4), the median f_{cov} of the FEASTS MW-like galaxies should also be ~ 0.8 dex higher than general MW-like galaxies. The median f_{cov} of the FEASTS MW-like galaxies for $\log(N_{\text{HI}}/\text{cm}^{-2}) > 17.8$ is ~ 0.04 (Figure 12-c), for an M_* -based virial radius estimate of 205 kpc. As a result, MW-like galaxies should have $f_{\text{cov}} \sim 0.006$ for $\log(N_{\text{HI}}/\text{cm}^{-2}) > 17.8$, roughly in agreement with the $f_{\text{cov}} \sim 0.01$ for $\log(N_{\text{HI}}/\text{cm}^{-2}) > 17.2$ at $z = 0$ predicted in Tortora et al. (2024) with the FIRE (Feedback In Realistic Environments, Hopkins et al. 2018) simulation.

We emphasize that, the above deductions assume that HI-poor galaxies follow similar N_{HI} distribution as HI-rich systems observed here. We await expansion of the FEASTS sample to low HI-richness systems in the near future, to confirm this result or otherwise.

7. SUMMARY

We derive the HI column density distribution function $f(N_{\text{HI}})$ down to a $\log(N_{\text{HI}}/\text{cm}^{-2}) \sim 17.8$, from 21-cm emission line column density maps at a resolution of 1 kpc for galaxies at $z = 0$. This analysis is based on a dataset of 21-cm HI images from the FEASTS and MHONGOOSE projects, for a sample of 65 galaxies that have M_{HI} ranging from 10^7 to $10^{10.7} M_{\odot}$, and M_* ranging from $10^{7.2}$ to $10^{11} M_{\odot}$. We find the following when comparing to previous $z \sim 0$ 21-cm emission line and quasar absorption observations:

1. $f(N_{\text{HI}})$ can be well fitted by a Schechter function in the $\log(N_{\text{HI}}/\text{cm}^{-2})$ range from 17.8 to 21, and is consistent with the Z05 result for the DLA regime.
2. The distribution of impact parameter b to the nearest galaxy for $\log(N_{\text{HI}}/\text{cm}^{-2}) > 17.8$ is tilted to significantly lower values than LLSs detected at $z < 0.5$, with median b being lower than 3 percentile of the LLS b , implying the complexity in associating absorbers to galaxies. The TNG50 prediction overestimates the b for the 25% most distant LLS-like HI around MW-like galaxies.
3. The N_{HI} radial distribution at $z = 0$ is most strongly correlated with r_{001} and r_{18} . We thus propose a method to infer M_{HI} for galaxies associated with LLSs.

We also find the following when comparing to previous quasar absorption observations at higher z :

1. The $f(N_{\text{HI}})$ at $z=0$ with a resolution of 1 kpc is comparable to or slightly lower than that of LLS (~ 1 pc) at $z \geq 3$

for $17.8 < \log(N_{\text{HI}}/\text{cm}^{-2}) < 19.2$, with the lower extent being larger if the cloud filling fraction is smaller. It is systematically lower by 0.1-0.4 dex than the latter for $19.2 < \log(N_{\text{HI}}/\text{cm}^{-2}) < 21$.

2. The $\log(N_{\text{HI}}/\text{cm}^{-2}) > 17.5$ length incidences inferred from combining the real HI images at $z = 0$ with HIMFs predicted at different redshifts are systematically higher by around 1.4 times than the LLS observed ones of $0.5 < z < 3$. This discrepancy indicates three possibilities of $z = 0$ versus $z > 0.5$ HI properties for tests in future studies: (1) the NUM predicted HIMFs under-estimates the galaxy densities by 1.4 times at $z > 0.5$, (2) $z = 0$ LLS cross-sections are 1.4 times higher than at higher redshift, (3) the average covering fraction of LLS clouds in 1-kpc areas that have LLS-like column densities is 70%.

ACKNOWLEDGMENTS

We gratefully thank X. Z. Chen for useful discussions. JW thanks support of the research grants from Ministry of Science and Technology of the People's Republic of China (NO. 2022YFA1602902), the National Natural Science Foundation of China (NO. 12073002), and the science research grants from the China Manned Space Project (NO. CMS-CSST-2021-B02). This work has received funding from the European Research Council (ERC) under the European Union's Horizon 2020 research and innovation programme (grant agreement No. 882793 "MeerGas"). LCH was supported by the National Natural Science Foundation of China (11721303, 11991052, 12011540375, 12233001), the National Key R&D Program of China (2022YFF0503401). PK is partially supported by the BMBF project 05A23PC1 for D-MeerKAT. Parts of this research were supported by High-performance Computing Platform of Peking University. DL thanks grants of NSFC (12588202). KN is supported by the MEXT/JSPS KAKENHI Grant Numbers JP22K21349, 24H00002, 24H00241 and 25K01032.

This work made use of the data from FAST (Five-hundred-meter Aperture Spherical radio Telescope, <https://cstr.cn/31116.02.FAST>). FAST is a Chinese national mega-science facility, operated by National Astronomical Observatories, Chinese Academy of Sciences.

Facilities: FAST: 500 m, VLA, WSRT, MeerKAT

Software: Astropy (Astropy Collaboration et al. 2013, 2018, 2022), numpy (van der Walt et al. 2011, v1.21.4), photutils (Bradley et al. 2019, v1.2.0), Python (Perez & Granger 2007, v3.9.13), scipy (Virtanen et al. 2020, 1.8.0)

APPENDIX

A. TABLE OF THE INTERFEROMETRIC DATA FOR THE FEASTS SAMPLE

We show in Figure 14 column density sensitivity as a function of angular and physical resolution for the initial

FEASTS+interferometric sample of 41 galaxies. We present in Table 2 the properties of the interferometric data collected

from past surveys or archives of interferometric telescopes for the finally analyzed FEASTS sample of 35 galaxies.

B. VERIFYING THE FAST BEAM UNIFICATION AND CLEAN PROCEDURE WITH MOCK TESTS

The multi-beam receivers on FAST and many other single-dish radio telescopes have significantly accelerated imaging surveys, through scanning the skies in drifting or on-the-fly mode. But when targeting low-surface-density structures, the images commonly have the problem of each beam of the multi-beam responds to the sky with different scattering patterns. They further share the problem of single-beam receivers that the beam response have side lobes and thus the shape deviates from a perfect Gaussian function, because of the blocking and diffraction of light. These problems hinder the scientific interpretation of low-surface-density structures detected in images. We have thus design procedures to unify and clean the beam for the diffuse HI images in section 3.1.2. The diffuse HI is the excess HI detected in a FAST image with respect to the corresponding interferometric image, and adding the diffuse HI image to the interferometric image produces the full HI image.

In the following, we conduct mock tests to verify the robustness of the beam unification and clean procedures in the final construction of full HI images.

We simulate the whole full-HI image constructing process, with a focus on correctly producing the diffuse HI image. The full-HI image (dense+diffuse HI) and the interferometric convolved model (dense HI) of each galaxy in the FEASTS sample are converted to have unit of Jy/arcsec, and used as the input images. They represent skies seen in the single-dish and interferometric mock observations, respectively. The mock observation, data processing, and final verification are conducted with the procedure described below. We use mock images built with the data of NGC 2903 as an example (left column of Figure 15).

The input full-HI image enters the FAST observing simulator, with noise added, and produces the mock observed FAST image. It is also directly convolved with the average beam (uB), and a Gaussian beam that has FWHM equal to $3'.24$ (gB), producing the reference FAST images. The input interferometric convolved model is convolved with the same synthesized interferometric beam, producing the mock observational interferometric image. By doing so, we miss the densest HI in the original data, but this HI does not affect processing of the diffuse HI. The three types of FAST images described above subtracting the mock observational interferometric image produce three observed diffuse HI images. The first one mimics the *observational* data with a *varied* and non-Gaussian beam (O(vB)), which is to be corrected. The remaining two images serve as the reference true images, one has a *uniform* but non-Gaussian beam (T(uB)), and the other has a *uniform* and *Gaussian* beam (T(gB)). They

are used to check the quality of beam unification and cleaning, respectively. In Figure 15, we can see that O(vB) deviate significantly from both T(uB) and T(gB).

We apply to O(vB) the beam unification procedure described in section 3.1.2, and obtain the beam unified image (O(uB)), as well as the correction image (C(vB→uB)). Figure 15 shows that, C(vB→uB) has similarly horizontal and vertical stripes as O(vB)-T(uB), but these artificial patterns mostly disappear in O(uB)-T(uB), indicating the success of beam unification. But T(uB)-T(gB) shows significant non-zero patterns, suggesting the necessity of applying the beam clean procedure.

We apply to O(uB) the beam clean procedure described in section 3.1.2, and obtain the clean model (M). The clean residual, $M * uB - O(uB)$, is relatively flat, indicating the success of deconvolution. The restored clean image $M * gB$ does not perfectly recover the T(gB), if the absolute residual is compared to the FAST image rms, reflecting challenges in deconvolution. However, the fraction residual with respect to fluxe in the reference full-HI image ($F(gB) = T(gB) + \text{mock observational interferometric image}$) is relatively small, mostly within 10% (or 0.04 dex).

We repeat the procedure above for all galaxies in the FEASTS sample, and reach similar conclusions. Three more examples are presented in the right column of Figure 15, and in Figure 16. The four example galaxies represent relatively isolated and interacting galaxies with interferometric data from the VLA (Figure 15) and WSRT (where HALOGAS was conducted, Figure 16), respectively. The NGC 4631 example shows the worst type of clean residual encountered in the whole sample, possibly because it is a strongly interacting edge-on galaxy that has a complex morphology. Yet the fractional residuals with respect to full-HI are acceptable.

The diffuse HI clean residuals discussed above are also the differences between recovered and reference full-HI images, because the mock interferometric images remain the same. Because the $f(N_{\text{HI}})$ counts areas in $\log(N_{\text{HI}}/\text{cm}^{-2})$ bins of 0.1-dex wide, the image recovery with typical systematic uncertainty less than 10% is satisfactory. Such a conclusion is further supported by the high level of consistency between the $f(N_{\text{HI}})$ derived with reference full-HI images (true) and that with recovered full-HI images (measure) in Figure 6.

C. THE $F(N_{\text{HI}})$ DATA POINTS AND SCHECHTER FUNCTION FITTING

Table 3 lists the data points and error bars for the $f(N_{\text{HI}})$ derived in this study.

Figure 17 shows the corner figure for the Schechter function fitting generated by the emcee procedure (Foreman-Mackey et al. 2013). It displays probability distributions in the parameter space, and the weak degeneracy between parameters. The final parameter f is the fractional systematic uncertainties of the model in describing the data, which is very small.

REFERENCES

Table 2. The interferometric data for the FEASTS sample (40 galaxies)

Name	Survey or archive	proj	array	b_{maj} (")	$\log N_{\text{HI,lim}}$ (cm^{-2})
(1)	(2)	(3)	(4)	(5)	(6)
IC1613	LITTLE THINGS	-	-	13.2	19.78
NGC1055	VLA	AG512	C (6.4h)	22.7	18.82
NGC2541	HALOGAS	-	-	17.5	19.42
NGC2841	THINGS	-	-	10.4	20.08
NGC2903	THINGS	-	-	16.5	19.73
NGC3198	HALOGAS	-	-	18.9	19.32
NGC3344	VLA	20A-125(B/C),21A-408(D)	B (27.8h), C (9.6h), D (2.5h)	12.6	18.39
NGC3486	VLA	13B-363 (B), 13A-107 (C)	B (2.7h) C (6.6h)	24.1	18.57
NGC3521	THINGS	-	-	15.9	19.88
NGC4214	THINGS	-	-	16.0	19.68
NGC4244	HALOGAS	-	-	21.1	19.28
NGC4254	VIVA	-	-	24.9	19.01
NGC4258	HALOGAS	-	-	18.6	19.46
NGC4395	VLA	AW619	B (19.7h), C (8.0h)	19.4	19.07
NGC4414	HALOGAS	-	-	25.9	19.22
NGC4449	VLA	AH540	D (2.1h)	60.7	18.58
NGC4490	VLA	AA181	C (5.9h), D (4.7h)	23.0	19.21
NGC4527	VLA	AM788	C (4.1h)	23.2	18.68
NGC4532	VIVA	-	-	19.3	18.94
NGC4536	VLA	AN119	C (6.8h)	20.9	18.96
NGC4559	HALOGAS	-	-	28.4	19.15
NGC4565	HALOGAS	-	-	31.8	19.08
NGC4618	VLA	AW618	B (14.3h), C (15.5h)	29.5	18.76
NGC4631	HALOGAS	-	-	33.7	19.16
NGC4656	VLA	AR215	D (4.8h)	54.6	19.22
NGC4826	THINGS	-	-	11.6	20.13
NGC5033	VLA	AP270	C (9.4h) D (4.6h)	27.9	18.50
NGC5055	HALOGAS	-	-	19.9	19.36
NGC5194	THINGS	-	-	11.0	20.09
NGC5248	VLA	AS787	C (2.9h)	20.4	19.34
NGC5457	THINGS	-	-	13.3	20.02
NGC5474	VLA	AH124	D (4.8h)	60.9	18.53
NGC5907	VLA	12A-405 (B), AS608 (C), AR302 (D)	B (21.2h) C (4.7h) D (0.6h) 22.3	18.96	
NGC628	THINGS	-	-	11.0	20.16
NGC660	VLA	AG230	C (7.2h), D(6.6h)	39.7	19.06
NGC672	HALOGAS	-	-	30.6	19.20
NGC7331	THINGS	-	-	7.5	20.50
NGC891	HALOGAS	-	-	23.4	19.02
NGC925	HALOGAS	-	-	25.3	19.20
SexB	LITTLE THINGS	-	-	17.9	19.52

Column (1): Galaxy name. Column (2): Survey name or the VLA archive, as origin of the interferometric data. Column (3): The project id of the data if the origin is the VLA archive. Column (4): The array configurations of data used, if the origin is the VLA archive. The on-source time is denoted in bracket after each configuration. Column (5): The major axis of the synthesized beam. Column (6): The column density limit ($3\text{-}\sigma$), quantified as the level of the $\log(N_{\text{HI}}/\text{cm}^{-2})$ contour where the median $S/N = 3$.

Table 3. The HI column density distribution function

$\log(N_{\text{HI}}/\text{cm}^{-2})$	$\log f(N_{\text{HI}})$	$\sigma(\log f(N_{\text{HI}}))$ (dex)
(1)	(2)	(3)
17.75	-19.20	0.06
17.85	-19.17	0.04
17.95	-19.26	0.04
18.05	-19.36	0.04
18.15	-19.47	0.04
18.25	-19.57	0.04
18.35	-19.68	0.04
18.45	-19.78	0.05
18.55	-19.88	0.04
18.65	-19.99	0.04
18.75	-20.10	0.04
18.85	-20.20	0.04
18.95	-20.29	0.04
19.05	-20.39	0.04
19.15	-20.48	0.04
19.25	-20.62	0.05
19.35	-20.77	0.04
19.45	-20.93	0.05
19.55	-21.05	0.04
19.65	-21.15	0.04
19.75	-21.26	0.04
19.85	-21.37	0.04
19.95	-21.48	0.04
20.05	-21.56	0.04
20.15	-21.65	0.04
20.25	-21.86	0.04
20.35	-22.03	0.04
20.45	-22.19	0.04
20.55	-22.35	0.05
20.65	-22.45	0.06
20.75	-22.57	0.05
20.85	-22.67	0.05
20.95	-22.80	0.05
21.05	-22.98	0.05
21.15	-23.25	0.04
21.25	-23.53	0.05
21.35	-23.79	0.08
21.45	-24.11	0.10
21.55	-24.47	0.12
21.65	-24.82	0.16
21.75	-24.98	0.18
21.85	-25.23	0.20
21.95	-25.80	0.28
22.05	-26.30	0.29
22.15	-28.42	1.32

Column (1): the center of HI column density bins. Column (2): the HI column density distribution function. Column (3): the error of the HI column density distribution function.

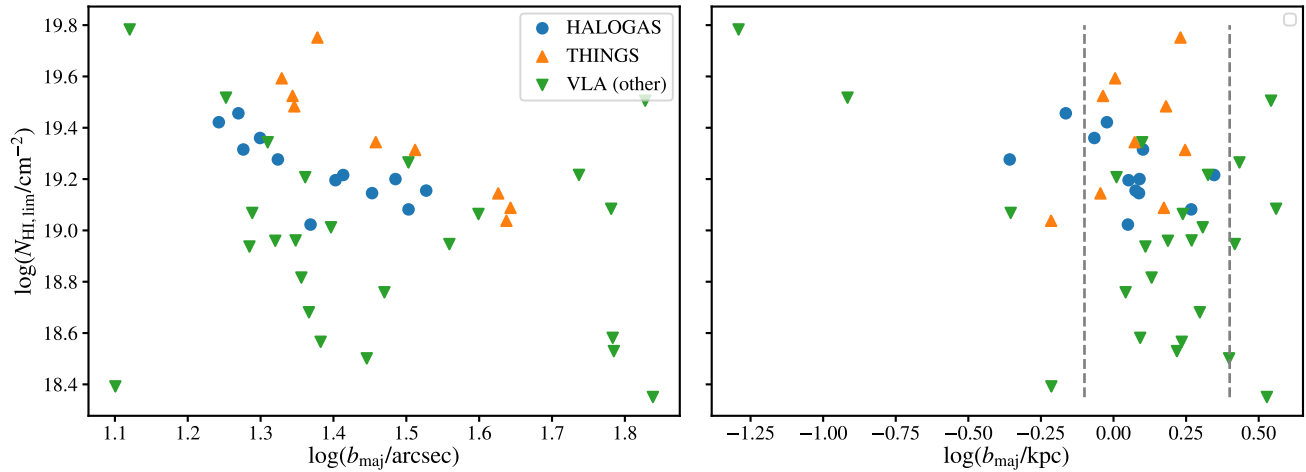


Figure 14. Depth and resolution of interferometry data for galaxies in the initial FEASTS+interferometric sample. The circles, upward triangles, and downward triangles are for data from the HALOGAS sample, the THINGS sample, and other VLA observed data. The left panel is a function of angular resolution; the right panel shows physical resolution. The two dashed vertical lines in the right panel enclose the range selected by this study, 0.8 to 2.4 kpc. Samples to the left of this range are downgraded to the resolution of 0.8 kpc, and samples to the right of this range are excluded from the final FEASTS sample.

- Agmon, N., Alhassid, Y., & Levine, R. D. 1979, *Journal of Computational Physics*, 30, 250
- Altay, G., Theuns, T., Schaye, J., Crighton, N. H. M., & Dalla Vecchia, C. 2011, *ApJL*, 737, L37
- Astropy Collaboration, Robitaille, T. P., Tollerud, E. J., et al. 2013, *A&A*, 558, A33
- Astropy Collaboration, Price-Whelan, A. M., Sipőcz, B. M., et al. 2018, *AJ*, 156, 123
- Astropy Collaboration, Price-Whelan, A. M., Lim, P. L., et al. 2022, *ApJ*, 935, 167
- Barton, E. J., & Cooke, J. 2009, *AJ*, 138, 1817
- Behroozi, P., Wechsler, R. H., Hearin, A. P., & Conroy, C. 2019, *MNRAS*, 488, 3143
- Bera, A., Kanekar, N., Chengalur, J. N., & Bagla, J. S. 2022, *ApJL*, 940, L10
- Bigiel, F., Leroy, A., Walter, F., et al. 2010, *AJ*, 140, 1194
- . 2008, *AJ*, 136, 2846
- Bradley, L., Sipőcz, B., Robitaille, T., et al. 2019, *astropy/photutils: v0.7.2*, Zenodo, doi:10.5281/zenodo.3568287
- Braun, R. 2012, *ApJ*, 749, 87
- Catinella, B., Saintonge, A., Janowiecki, S., et al. 2018, *MNRAS*, 476, 875
- Chen, H.-W., Helsby, J. E., Gauthier, J.-R., et al. 2010, *ApJ*, 714, 1521
- Chen, H.-W., Zahedy, F. S., Boettcher, E., et al. 2020, *MNRAS*, 497, 498
- Chen, H.-W., Qu, Z., Rauch, M., et al. 2023, *ApJL*, 955, L25
- Chen, X., Ching, T.-C., Li, D., et al. 2025, *AJ*, 169, 158
- Chowdhury, A., Kanekar, N., & Chengalur, J. N. 2022a, *ApJL*, 935, L5
- . 2022b, *ApJL*, 941, L6
- Chowdhury, A., Kanekar, N., Chengalur, J. N., Sethi, S., & Dwarakanath, K. S. 2020, *Nature*, 586, 369
- Chung, A., van Gorkom, J. H., Kenney, J. D. P., Crowl, H., & Vollmer, B. 2009, *AJ*, 138, 1741
- Crain, R. A., Bahé, Y. M., Lagos, C. d. P., et al. 2017, *MNRAS*, 464, 4204
- Davé, R., Crain, R. A., Stevens, A. R. H., et al. 2020, *MNRAS*, 497, 146
- de Blok, W. J. G., Healy, J., Maccagni, F. M., et al. 2024, *A&A*, 688, A109
- Diemer, B., Stevens, A. R. H., Forbes, J. C., et al. 2018, *ApJS*, 238, 33
- Faucher-Giguère, C.-A. 2020, *MNRAS*, 493, 1614
- Faucher-Giguère, C.-A., Feldmann, R., Quataert, E., et al. 2016, *MNRAS*, 461, L32
- Faucher-Giguère, C.-A., Hopkins, P. F., Kereš, D., et al. 2015, *MNRAS*, 449, 987
- Foreman-Mackey, D., Hogg, D. W., Lang, D., & Goodman, J. 2013, *PASP*, 125, 306
- Fumagalli, M., Hennawi, J. F., Prochaska, J. X., et al. 2014, *ApJ*, 780, 74
- Fumagalli, M., O’Meara, J. M., Prochaska, J. X., & Worseck, G. 2013, *ApJ*, 775, 78
- Fumagalli, M., Patel, S. G., Franx, M., et al. 2012, *ApJL*, 757, L22
- Gronke, M., & Oh, S. P. 2020, *MNRAS*, 494, L27

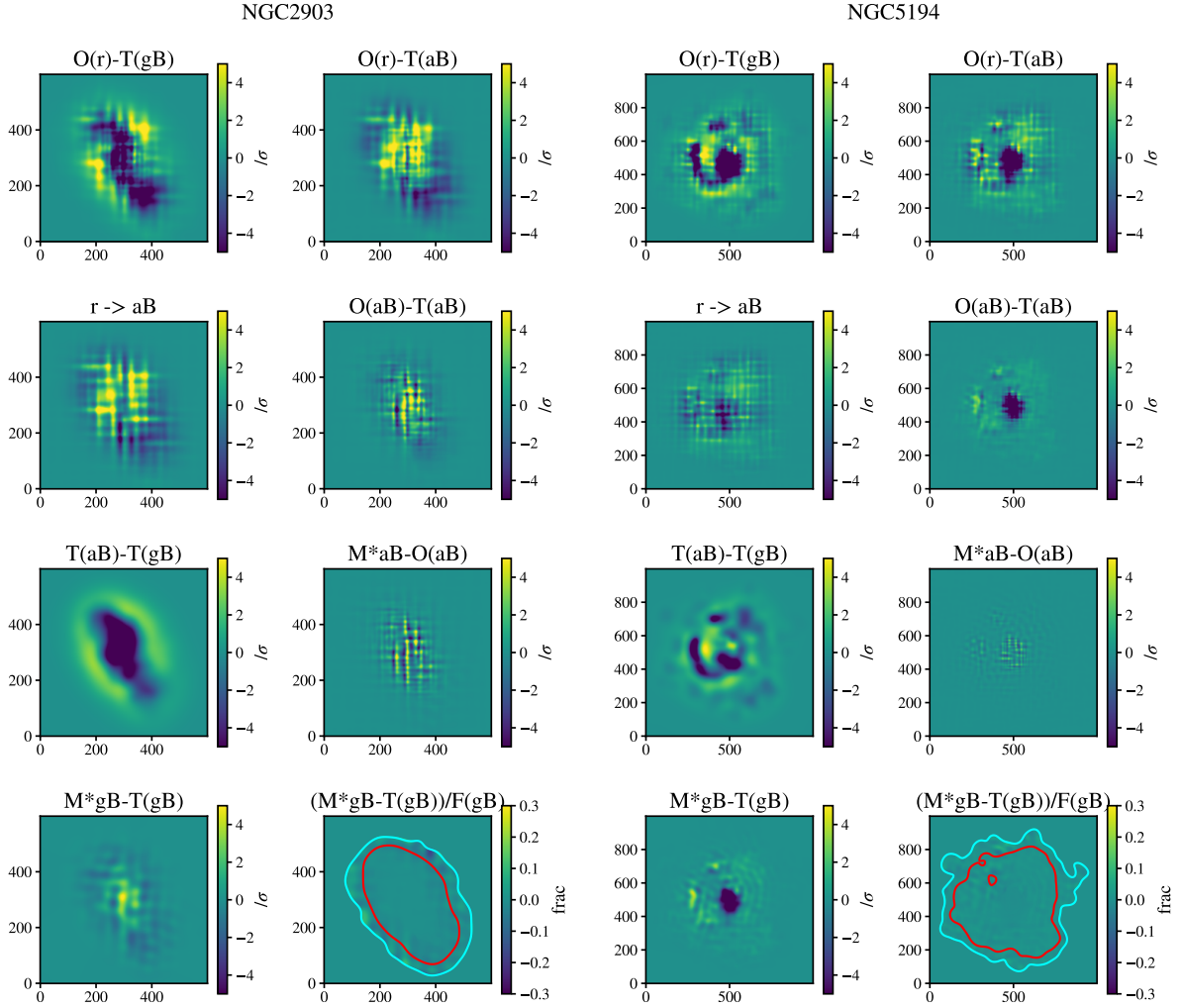


Figure 15. Example mock test galaxies, for which the input interferometric data are from the VLA. The left and right two columns are for two mock galaxies respectively. Please refer to Appendix B for detailed explanation of the image titles.

Guo, H., Wang, J., Jones, M. G., & Behroozi, P. 2023, *ApJ*, 955, 57
 Heald, G., Józsa, G., Serra, P., et al. 2011, *A&A*, 526, A118
 Hoffman, G. L., Dowell, J., Haynes, M. P., & Giovanelli, R. 2019, *AJ*, 157, 194
 Hopkins, P. F., Wetzell, A., Kereš, D., et al. 2018, *MNRAS*, 480, 800
 Huang, Q., Wang, J., Lin, X., et al. 2025, *ApJ*, 980, 157
 Hunter, D. A., Ficut-Vicas, D., Ashley, T., et al. 2012, *AJ*, 144, 134
 Ji, S., Chan, T. K., Hummels, C. B., et al. 2020, *MNRAS*, 496, 4221
 Jiang, P., Yue, Y., Gan, H., et al. 2019, *Science China Physics, Mechanics, and Astronomy*, 62, 959502
 Kacprzak, G. G., Churchill, C. W., Steidel, C. C., & Murphy, M. T. 2008, *AJ*, 135, 922
 Kanekar, N., Braun, R., & Roy, N. 2011, *ApJL*, 737, L33
 Karachentsev, I. D., Makarov, D. I., & Kaisina, E. I. 2013, *AJ*, 145, 101

Kim, T. S., Carswell, R. F., Cristiani, S., D’Odorico, S., & Giallongo, E. 2002, *MNRAS*, 335, 555
 Koch, E. W., Rosolowsky, E. W., Leroy, A. K., et al. 2021, *MNRAS*, 504, 1801
 Kourkchi, E., & Tully, R. B. 2017, *ApJ*, 843, 16
 Kroupa, P. 2001, *MNRAS*, 322, 231
 Lagos, C. D. P., Baugh, C. M., Zwaan, M. A., et al. 2014, *MNRAS*, 440, 920
 Lanzetta, K. M., Wolfe, A. M., Turnshek, D. A., et al. 1991, *ApJS*, 77, 1
 Leroy, A. K., Walter, F., Brinks, E., et al. 2008, *AJ*, 136, 2782
 Leroy, A. K., Sandstrom, K. M., Lang, D., et al. 2019, *ApJS*, 244, 24
 Lin, X., Wang, J., Kauffmann, G., Springel, V., & Pakmor, R. 2025, *ApJ*, arXiv:2502.10672
 Lucy, L. B. 1974, *AJ*, 79, 745
 Ma, W., Guo, H., Xu, H., et al. 2025, *A&A*, 695, A241

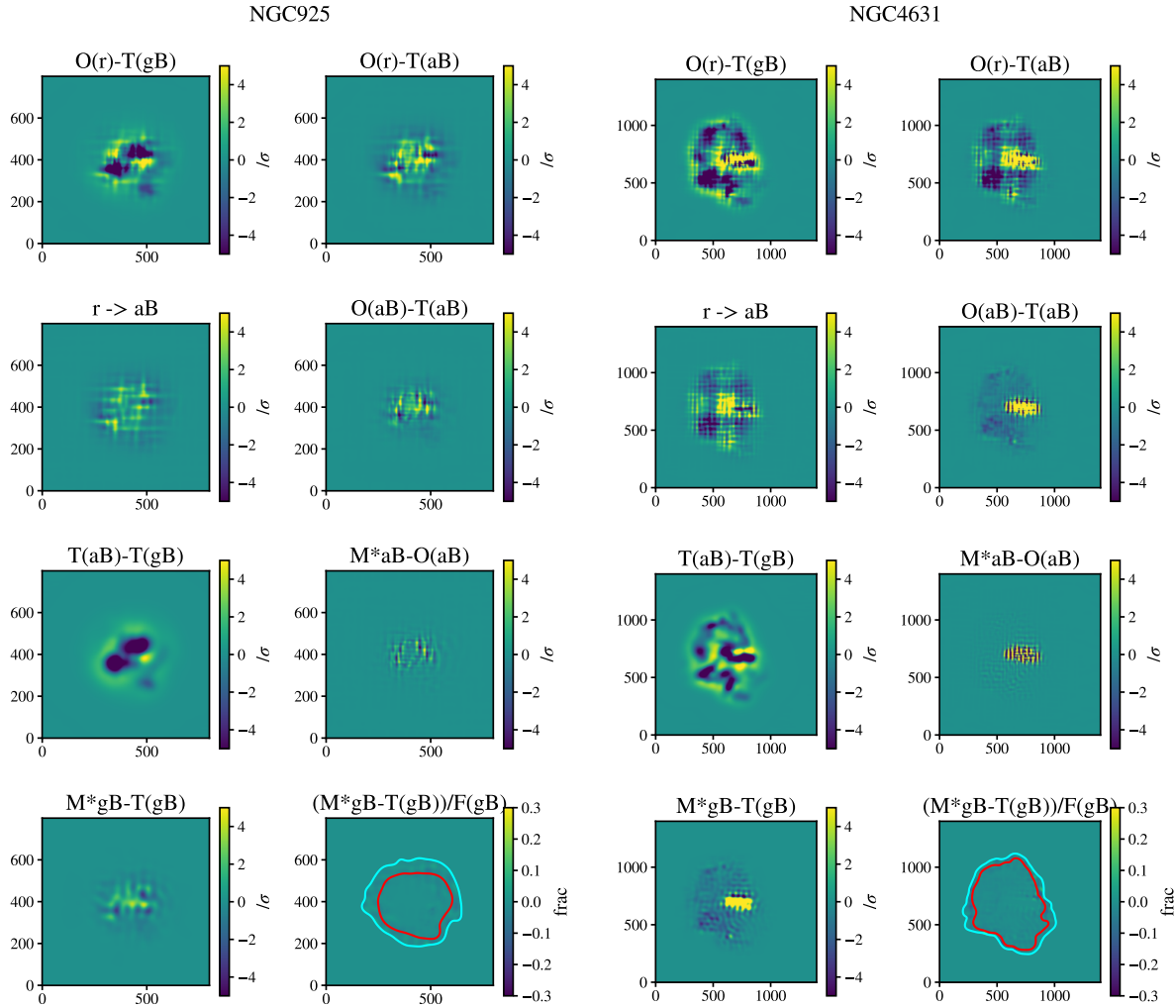


Figure 16. Example mock test galaxies. Similar to Figure 15, but with the input interferometric data are from the WSRT (HALOGAS).

Marasco, A., de Blok, W. J. G., Maccagni, F. M., et al. 2025, *A&A*, 697, A86

Marinacci, F., Grand, R. J. J., Pakmor, R., et al. 2017, *MNRAS*, 466, 3859

Nagamine, K., Choi, J.-H., & Yajima, H. 2010, *ApJL*, 725, L219

Nelson, D., Pillepich, A., Springel, V., et al. 2019, *MNRAS*, 490, 3234

Noterdaeme, P., Petitjean, P., Carithers, W. C., et al. 2012, *A&A*, 547, L1

O’Meara, J. M., Prochaska, J. X., Worseck, G., Chen, H.-W., & Madau, P. 2013, *ApJ*, 765, 137

Pan, H., Jarvis, M. J., Santos, M. G., et al. 2023, *MNRAS*, 525, 256

Paturel, G., Theureau, G., Bottinelli, L., et al. 2003, *A&A*, 412, 57

Perez, F., & Granger, B. E. 2007, *Computing in Science and Engineering*, 9, 21

Péroux, C., & Howk, J. C. 2020, *ARA&A*, 58, 363

Péroux, C., Weng, S., Karki, A., et al. 2022, *MNRAS*, 516, 5618

Pillepich, A., Nelson, D., Springel, V., et al. 2019, *MNRAS*, 490, 3196

Pingel, N. M., Chen, H., Stanimirović, S., et al. 2024, *ApJ*, 974, 93

Prochaska, J. X., Hennawi, J. F., & Simcoe, R. A. 2013a, *ApJL*, 762, L19

Prochaska, J. X., O’Meara, J. M., & Worseck, G. 2010, *ApJ*, 718, 392

Prochaska, J. X., Hennawi, J. F., Lee, K.-G., et al. 2013b, *ApJ*, 776, 136

Qu, Z., Chen, H.-W., Schiller, E., Wang, J., & Gronke, M. 2025, *arXiv e-prints*, arXiv:2512.12958

Qu, Z., Chen, H.-W., Rudie, G. C., et al. 2023, *MNRAS*, 524, 512

Rahmati, A., Pawlik, A. H., Raičević, M., & Schaye, J. 2013a, *MNRAS*, 430, 2427

Rahmati, A., Schaye, J., Bower, R. G., et al. 2015, *MNRAS*, 452, 2034

Rahmati, A., Schaye, J., Pawlik, A. H., & Raičević, M. 2013b, *MNRAS*, 431, 2261

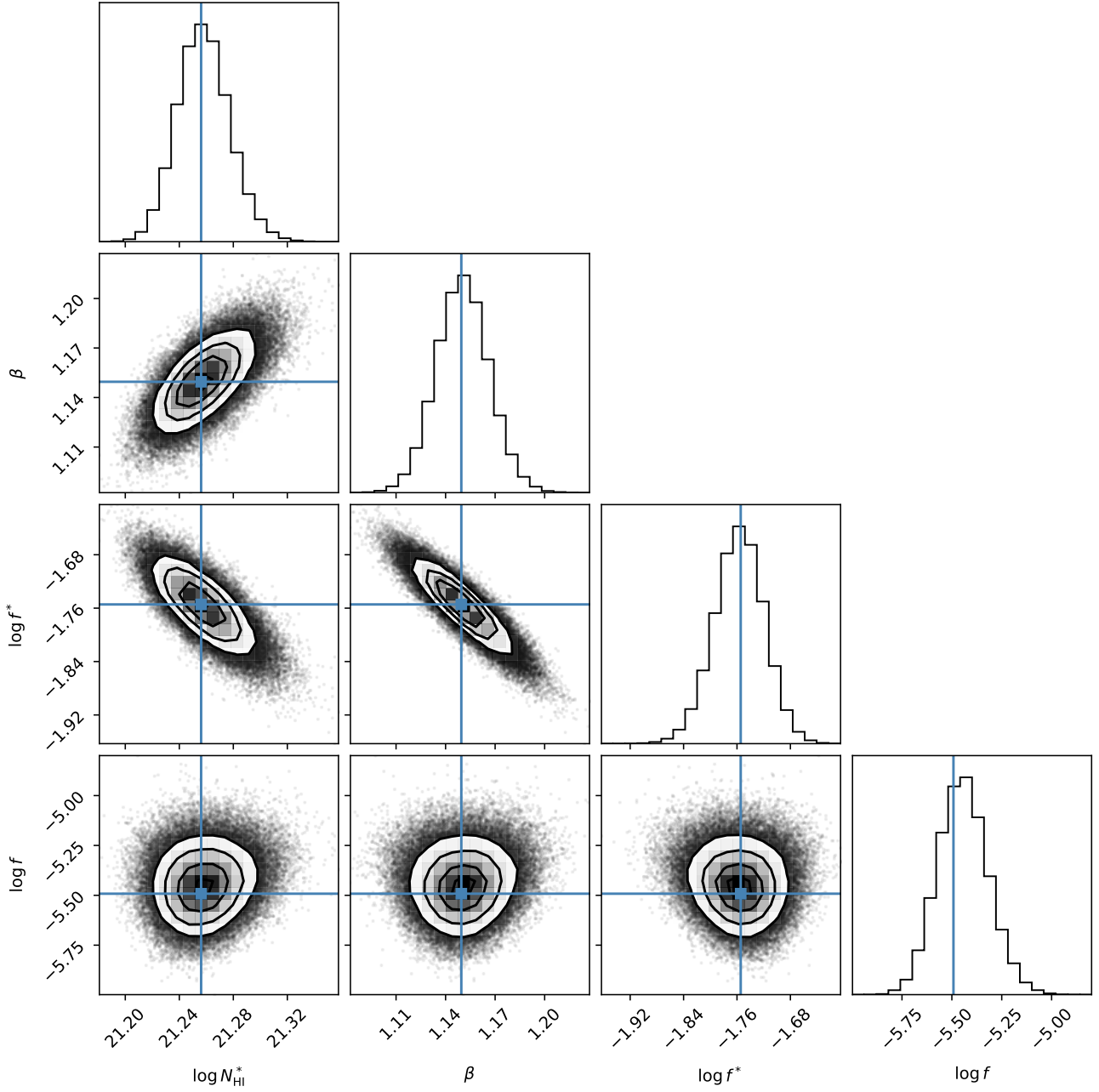


Figure 17. Schechter function fitting for the $f(N_{\text{HI}})$ measurements. The parameters $\lg N_{\text{HI}}^*$, β and $\log f^*$ together form the Schechter function displayed in Equation 2. The f of $\log f$ describes the fractional level of variance underestimation. It plots all the one and two dimensional projections of the posterior probability distributions of parameters, with prior distributions described in the main text (Section 5). The best-fit values (from `scipy.optimize`) are marked as vertical and horizontal lines.

- Ribaldo, J., Lehner, N., & Howk, J. C. 2011, *ApJ*, 736, 42
- Richardson, W. H. 1972, *Journal of the Optical Society of America* (1917-1983), 62, 55
- Rudie, G. C., Steidel, C. C., Trainor, R. F., et al. 2012, *ApJ*, 750, 67
- Ryan-Weber, E. V., Webster, R. L., & Staveley-Smith, L. 2003, *MNRAS*, 343, 1195
- Saintonge, A., & Catinella, B. 2022, *ARA&A*, 60, 319
- Saintonge, A., Catinella, B., Cortese, L., et al. 2016, *MNRAS*, 462, 1749
- Schaye, J., Dalla Vecchia, C., Booth, C. M., et al. 2010, *MNRAS*, 402, 1536
- Schaye, J., Crain, R. A., Bower, R. G., et al. 2015, *MNRAS*, 446, 521
- Schechter, P. 1976, *ApJ*, 203, 297
- Serra, P., Westmeier, T., Giese, N., et al. 2015, *MNRAS*, 448, 1922
- Sinigaglia, F., Rodighiero, G., Elson, E., et al. 2022, *ApJL*, 935, L13
- Sokoliuk, O., Webb, J. K., Lanzetta, K. M., et al. 2025, *arXiv e-prints*, arXiv:2510.07259
- Songaila, A., & Cowie, L. L. 2010, *ApJ*, 721, 1448
- Stanimirovic, S. 2002, in *Astronomical Society of the Pacific Conference Series*, Vol. 278, *Single-Dish Radio Astronomy: Techniques and Applications*, ed. S. Stanimirovic, D. Altschuler, P. Goldsmith, & C. Salter, 375–396
- Stern, J., Sternberg, A., Faucher-Giguère, C.-A., et al. 2021, *MNRAS*, 507, 2869
- Stevens, A. R. H., Diemer, B., Lagos, C. d. P., et al. 2019, *MNRAS*, 483, 5334
- Storrie-Lombardi, L. J., McMahon, R. G., Irwin, M. J., & Hazard, C. 1994, *ApJL*, 427, L13
- Suresh, J., Nelson, D., Genel, S., Rubin, K. H. R., & Hernquist, L. 2019, *MNRAS*, 483, 4040
- Tillman, M. T., Burkhart, B., Tonnesen, S., et al. 2023, *AJ*, 166, 228
- Tortora, L., Feldmann, R., Bernardini, M., & Faucher-Giguère, C.-A. 2024, *MNRAS*, 532, 3847
- van de Voort, F., Schaye, J., Altay, G., & Theuns, T. 2012, *MNRAS*, 421, 2809
- van de Voort, F., Springel, V., Mandelker, N., van den Bosch, F. C., & Pakmor, R. 2019, *MNRAS*, 482, L85
- van der Walt, S., Colbert, S. C., & Varoquaux, G. 2011, *Computing in Science and Engineering*, 13, 22
- Villaescusa-Navarro, F., Genel, S., Castorina, E., et al. 2018, *ApJ*, 866, 135
- Virtanen, P., Gommers, R., Oliphant, T. E., et al. 2020, *Nature Methods*, 17, 261
- Walter, F., Brinks, E., de Blok, W. J. G., et al. 2008, *AJ*, 136, 2563
- Walter, F., Carilli, C., Neeleman, M., et al. 2020, *ApJ*, 902, 111
- Wang, J., Yang, D., Oh, S. H., et al. 2023, *ApJ*, 944, 102
- Wang, J., Lin, X., Yang, D., et al. 2024a, *ApJ*, 968, 48
- Wang, J., Lin, X., Staveley-Smith, L., et al. 2024b, *ApJ*, 973, 15
- Wang, J., Yang, D., Lin, X., et al. 2025, *ApJ*, 980, 25
- Weng, S., Péroux, C., Ramesh, R., et al. 2024, *MNRAS*, 527, 3494
- Weng, S., Péroux, C., Karki, A., et al. 2023, *MNRAS*, 519, 931
- Westmeier, T., Kitaeff, S., Pallot, D., et al. 2021, *MNRAS*, 506, 3962
- Yajima, H., Choi, J.-H., & Nagamine, K. 2012, *MNRAS*, 427, 2889
- Yang, D., Wang, J., Qu, Z., et al. 2025, *ApJ*, 984, 15
- Zafar, T., Péroux, C., Popping, A., et al. 2013, *A&A*, 556, A141
- Zwaan, M. A., Meyer, M. J., Staveley-Smith, L., & Webster, R. L. 2005a, *MNRAS*, 359, L30
- Zwaan, M. A., van der Hulst, J. M., Briggs, F. H., Verheijen, M. A. W., & Ryan-Weber, E. V. 2005b, *MNRAS*, 364, 1467
- Zwaan, M. A., Staveley-Smith, L., Koribalski, B. S., et al. 2003, *AJ*, 125, 2842